SANDIA REPORT

SAND2005-4749
Unlimited Release
Printed August 2005

Studies on the Disbonding Initiation of Interfacial Cracks

Brian J. McAdams, Raymond A. Pearson, Lehigh University

Prepared by
Sandia National Laboratories
Albuquerque, New Mexico 87185 and Livermore, California 94550

Sandia is a multiprogram laboratory operated by Sandia Corporation,
a Lockheed Martin Company, for the United States Department of Energy's
National Nuclear Security Administration under Contract DE-AC04-94AL85000.

Issued by Sandia National Laboratories, operated for the United States Department of Energy by Sandia Corporation.

Available to DOE and DOE contractors from
U.S. Department of Energy
Office of Scientific and Technical Information
P.O. Box 62
Oak Ridge, TN 37831

Telephone: (865)576-8401
Facsimile: (865)576-5728
E-Mail: reports@adonis.osti.gov
Online ordering: http://www.osti.gov/bridge

Available to the public from
U.S. Department of Commerce
National Technical Information Service
5285 Port Royal Rd
Springfield, VA 22161

Telephone: (800)553-6847
Facsimile: (703)605-6900
E-Mail: orders@ntis.fedworld.gov
Online order: http://www.ntis.gov/help/ordermethods.asp?loc=7-4-0#online

SAND2005-4749
Unlimited Release
Printed August 2005

STUDIES ON THE DISBONDING INITIATION OF INTERFACIAL CRACKS

Brian J. McAdams
Raymond A. Pearson
Center for Polymer Science and Engineering
Department of Material Science and Engineering
Lehigh University, Bethlehem, PA 18015

ABSTRACT

With the continuing trend of decreasing feature sizes in flip-chip assemblies, the reliability tolerance to interfacial flaws is also decreasing. Small-scale disbonds will become more of a concern, pointing to the need for a better understanding of the initiation stage of interfacial delamination. With most accepted adhesion metric methodologies tailored to predict failure under the prior existence of a disbond, the study of the initiation phenomenon is open to development and standardization of new testing procedures. Traditional fracture mechanics approaches are not suitable, as the mathematics assume failure to originate at a disbond or crack tip. Disbond initiation is believed to first occur at free edges and corners, which act as high stress concentration sites and exhibit singular stresses similar to a crack tip, though less severe in intensity. As such, a "fracture mechanics-like" approach may be employed which defines a material parameter - a critical stress intensity factor (K_C) - that can be used to predict when initiation of a disbond at an interface will occur.

The factors affecting the adhesion of underfill/polyimide interfaces relevant to flip-chip assemblies were investigated in this study. The study consisted of two distinct parts: a comparison of the initiation and propagation phenomena and a comparison of the relationship between sub-critical and critical initiation of interfacial failure. The initiation of underfill interfacial failure was studied by characterizing failure at a free-edge with a critical stress intensity factor. In comparison with the interfacial fracture toughness testing, it was shown that a good correlation exists between the initiation and propagation of interfacial failures. Such a correlation justifies the continuing use of fracture mechanics to predict the reliability of flip-chip packages. The second aspect of the research involved fatigue testing of tensile butt joint specimens to determine lifetimes at sub-critical load levels. The results display an interfacial strength ranking similar to that observed during monotonic testing. The fatigue results indicate that monotonic fracture mechanics testing may be an adequate screening tool to help predict cyclic underfill failure; however lifetime data is required to predict reliability.

The work discussed in this report was supported by a Campus Executive Fellowship LDRD.

CHAPTER 1 – INTRODUCTION

1.1 Flip Chip Technology

One of the more significant microelectronics packaging developments to improve on size, cost, power, and reliability has been the development of flip chip technology [1]. Originally invented by IBM in the 1960s as controlled collapse chip connection (C4), the process involves inverting a solder bumped silicon die (active face down) and attaching it directly to the chip carrier instead of the more-traditional method of wire bonding connections from the silicon die perimeter (see Figure 1.1). Since the interconnections can be directly bonded in area arrays to the active devices on the chip rather than routed to the periphery, the technology allows for more input/output (I/O) connections and smaller die sizes than wirebonding technology. Additionally, the direct interconnection provides shorter I/O paths and higher transmission speed.

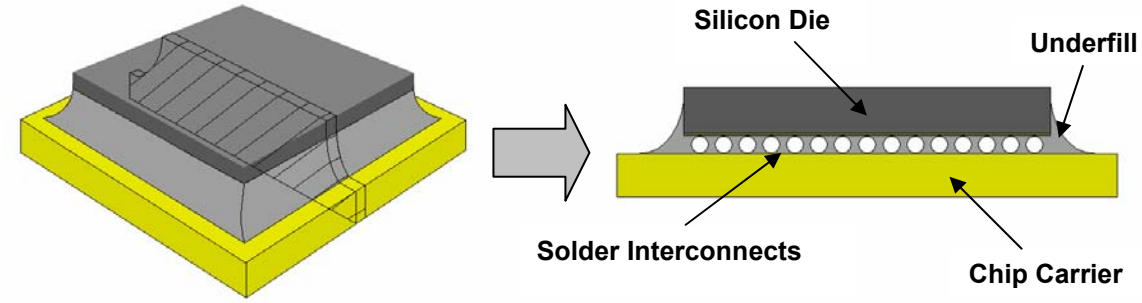

Figure 1.1: Cross-section of a flip-chip package.

The original flip-chip process was implemented for ceramic substrates, with coefficients of thermal expansion (CTEs) of about 4-8ppm/°C that were a good match to the CTE of silicon (3ppm/°C). As organic substrates emerged in the 1990s as a cheaper alternative, the mismatch of the CTEs (15-30ppm/°C for the organic chip carriers) became a critical reliability concern. This thermal mismatch resulted in significantly high shear stresses being placed on the solder interconnections during the lifetime of the package [2]:

$$\varepsilon_{Outer} = \frac{d[(CTE_{Substrate}\Delta T_{Substrate}) - ((CTE_{Silicon}\Delta T_{Silicon}))]}{h} \qquad \textbf{(1.1)}$$

where ε_{Outer} is the strain in the outer most solder interconnection, d is the distance to the center of the package, h is the height of the interconnects, and ΔT is the change in temperature that the package experiences. To compensate for this mismatch, it was found that underfilling the gap left by the solder interconnections with an epoxy resin could couple the chip and substrate to help manage the stresses with a tremendous increase in reliability [3].

1.2 Flip Chip Reliability

With the underfill layer locally constraining the CTE mismatch, the primary reliability issue for flip-chip technology is underfill delamination, which results in a decoupling of the chip and substrate and subsequent solder fatigue [4]. Though other failure modes such as die cracking and solder migration exist, it is the strength of the underfill interfaces that often dictates flip-chip lifetimes. Such interfacial failure is expected to originate at one of the several material or geometric discontinuities that serve as stress concentrations in the package (see Figure 1.2).

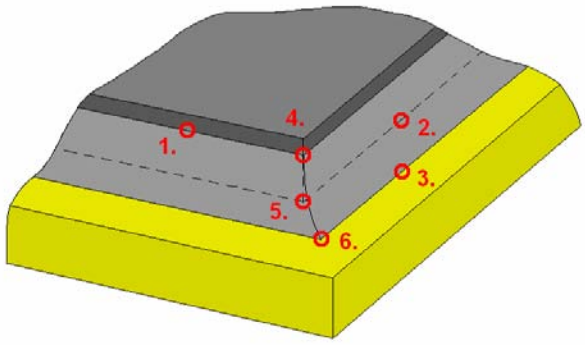

Figure 1.2: Locations of interfacial failure in a typical flip-chip package.

Termed as singularities, the mathematical representation of the stress fields at these locations approach infinity as follows:

$$\sigma = Kr^{-(\lambda-1)} \qquad \textbf{(1.2)}$$

where K is the magnitude of the stress field (called the stress intensity factor), r is the distance from the singularity, and λ-1 is the order or strength of the singularity. The relative severity of these singular locations is defined by how quickly these stresses approach the asymptotic infinity, as can be seen by the magnitude of the exponent, λ-1.

Looking at Figure 1.2, there are six distinct singularities where underfill failure can occur: 1). the top edge of the underfill fillet bonded to the silicon chip, 2). the passivated bottom edge of the silicon chip bonded to the underfill, 3). the bottom edge of the underfill fillet bonded to the circuit carrier, 4). the top corner of underfill fillet bonded to the silicon die, 5). the passivated bottom corner of silicon die bonded to the underfill, and 6). the bottom corner of underfill fillet bonded to the circuit carrier. By examining the strength of the singular stress field at each of these locations for a flip chip assembly mounted to a FR4 printed circuit board, it can be shown that 3-D corners (sites 4, 5 and 6) are more likely to fail than edge singularities (sites 1, 2, and 3), with the strength of singularity for the fillet locations (1, 3, 4, and 6) heavily dependent on the fillet angle. The most severe stress singularity (in the absence of an interfacial flaw) is expected to occur at the embedded bottom corner of the silicon die [5].

As can be expected by the severity of the embedded corner (site 5), it is the interface between the underfill and the die passivation layer that often seems to show the highest tendency for delamination [6]. Reliability studies of polyimide-passivated flip-chip packages subjected to cyclic thermal excursions often show delamination at the underfill/polyimide interface (see Figure 1.3).

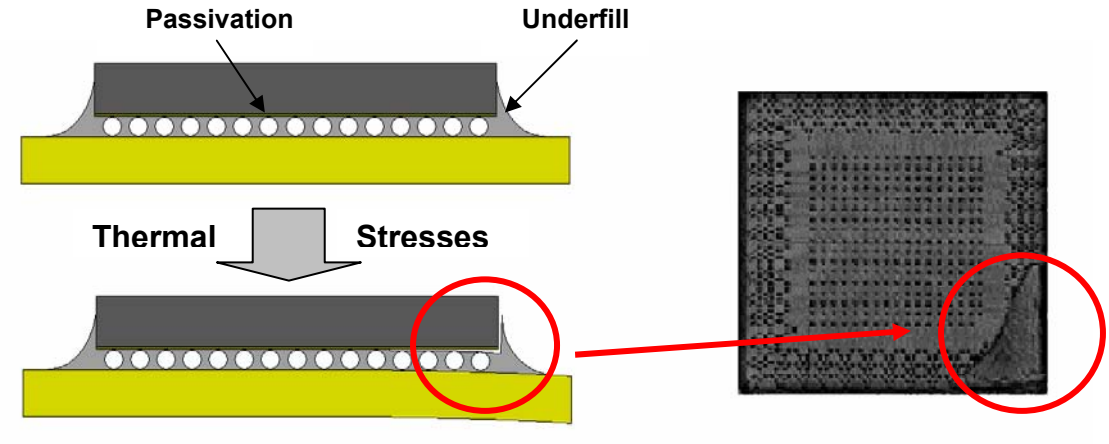

Figure 1.3: Delamination at the underfill/passivation interface detected by scanning acoustic microscopy (C-SAM image courtesy of D. Peterson, Sandia National Labs).

The International Technology Roadmap for Semiconductors (ITRS) continues to highlight the need for a better understanding of flip-chip underfill interfacial behavior as an area critical to future chip development and manufacturing. [1]:

> *"Interfacial delamination will continue to be a critical reliability hazard that is worsened by the trend to larger chips and new materials. Standard methods and acceptance criteria for interfacial adhesion are lacking. Fundamental work is needed to establish adhesion strength and degradation rate versus environmental factors as well as a function of interfacial physical and chemical properties. Assembly and packaging thermal performance, reliability and cost are driven by understanding of interfaces and ability to characterize, control, and strengthen them."*

2.1.1 Interfacial Adhesion

The toughness of an interface is essentially the energy required to separate the two adjoining materials, typically quantified in terms of a critical energy release rate for crack extension along the interface (G_c), measured in units of energy per unit area. In theory, when the release of stored strain energy is equal to or greater than the thermodynamic work of adhesion (W_A), fracture can take place with the formation of new free crack surfaces. However, the interfacial fracture energy of a real system is generally several orders of magnitude higher than the thermodynamic work of adhesion, where the excess energy (G_c-W_A) is lost through material dissipative mechanisms. Formation of free surface area at the interface is primarily determined by two different energy absorbing processes: the work required to break the interfacial bonds and the energy adsorbed by viscoelastic, plastic and toughening processes in the materials at the tip and wake of the advancing interface crack (see Figure 2.1).

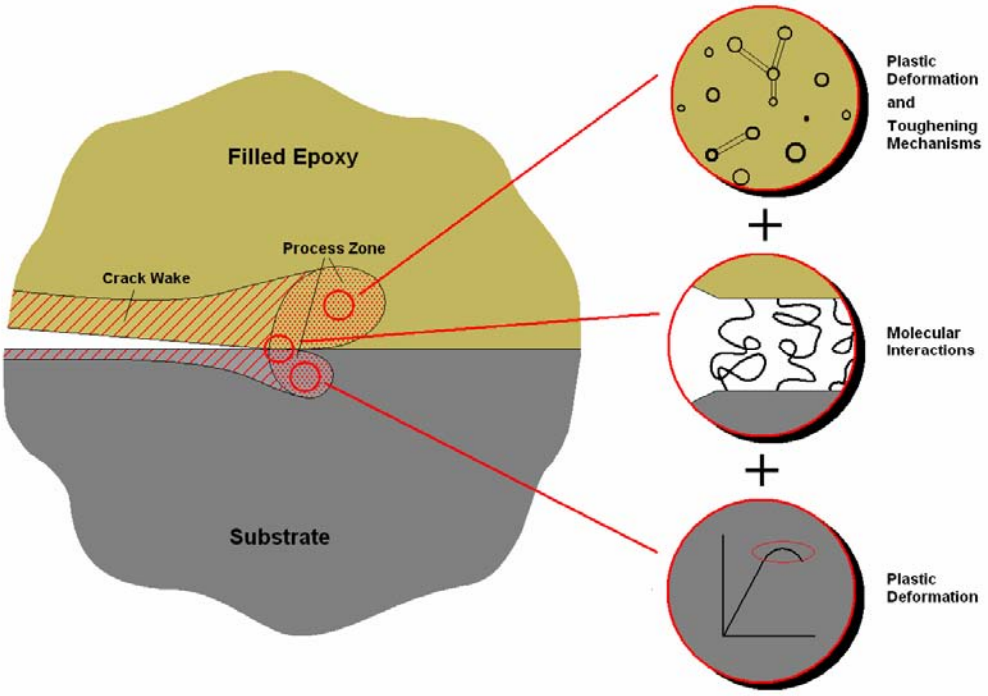

Figure 2.1: Factors of adhesion (filled epoxy bonded to a ductile substrate).

This was first demonstrated by Gent and Schultz, who found that during peel testing of polybutadiene, the observed peel strength was higher than that predicted by thermodynamic considerations and was strongly dependant on the rate of peeling [7]. They proposed that the peel strength was in fact the product of two terms: the thermodynamic molecular interactions and a second term which represented the energy adsorbed through viscoelastic processes. This viscoelastic contribution was also seen by Andrews and Kinloch, who studied the peel strength

of a styrene and butadiene copolymer to several polymeric substrates [8, 9]. Maugis and Barquins performed similar testing of polyurethane to glass and proposed the following relation for adherence of glass-elastomer interfaces [10]:

$$G_c = W_A\left[1+\phi(a_T, v)\right] \qquad \textbf{(2.1)}$$

where G_c is the critical strain energy release rate, W_A is the thermodynamic work of adhesion, which is dependant on the molecular interactions at the interface, and $\phi(a_T, v)$ is a function characteristic of the viscoelastic losses at the crack tip. The viscoelastic contribution was found to be proportional to the work of adhesion and be dependant on temperature (by the shift factor, a_T) and crack growth rate (v). The excess energy dissipation can be seen to be dependent on the strength of the molecular interactions, with $G_c - W_A = W_A\phi(a_T, v)$. More recent work by Cho *et al.* and Creton *et al.* on block copolymers and have shown that both viscoelastic and plastic deformation have a similar effect of increasing the interfacial fracture of glassy polymers [11, 12]. Xu *et al.* proposed a similar equation to (2.3) for viscoelastic polymers using a fracture mechanics model [13]:

$$G_c = G_{AD}\left[1+\phi(a_T, v, c)\right] \qquad \textbf{(2.2)}$$

where G_{AD} is the intrinsic fracture toughness of the interface (dictated by the molecular interactions), and $\phi(a_T, v, c)$ is the same as for equation (2.3) however also includes a weak dependency on specimen geometry (c). In a similar study, Evans *et al.* concluded that for various bimaterial interfaces, the difference between measured interfacial fracture energy and the work of adhesion was due to roughness effects, as well as viscoelastic and plastic energy dissipation [14]. Relatively recent unpublished work by Komnopad *et al.* has able to show a distinct interplay between the strength of molecular interactions and bulk fracture toughness [15, 16]. The study examined the effect of altering the bulk fracture toughness through different modifiers of an epoxy system on interfacial strength. The results indicated that when the molecular interactions at an interface are constant (identical epoxy matrix), the toughest material displays the best adhesion (see Table 2.1).

Table 2.1: Bulk vs. interfacial (to polyimide) properties for an epoxy system with different toughening modifiers [15].

Epoxy	*Bulk Gc (J/m^2)*	*Inter. Gc (J/m^2)* $\psi_{r=0.01mm}$ *= -8°*
Neat	300	160
10% CTBN	3580	2930
10% Solid Glass Sphere	890	1530
5% CTBN/5% Solid Glass Spheres	2020	1490

For different epoxy materials with varying molecular interactions, the toughest material did not always display the largest adhesion strength (Table 2.2). This was attributed to insufficient

interfacial interactions for the bulk deformation mechanisms to operate at the interface (poor load transfer).

Table 2.2: Bulk vs. interfacial properties for three different epoxy systems with diffferent bulk fracture toughness [16].

Epoxy	*Bulk Gc (J/m²)*	*Inter. Gc (J/m²)* $\psi_{r=0.01mm} = -8°$
Dexter	516	19
Zymet	196	63
Ablestik	540	37

2.2 Interfacial Fracture Mechanics

With underfill adhesion such a critical reliability issue, a means of quantifying interfacial strength has become a necessary tool to the development of flip-chip packages. Given that microelectronics packaging lifetimes are often governed by interfacial fracture phenomena, significant work has gone into developing reliability testing based on fracture mechanics. Predictions for interfacial failure using fracture mechanics rely on critical fracture parameters that characterize either the stress field at a crack tip or an energy release rate as the driving force for crack propagation. From either the stress or energy approach, adhesion can be quantified by an interfacial fracture toughness value, determined from a K-calibration relationship for the relevant geometry. These are typically deduced functional form solutions where some parameters are chosen based on finite element results.

Starting from the context of a homogeneous, isotropic elastic solid, a relation for the critical stress required for crack propagation was originally proposed by Griffith [17], and modified to include the plastic deformations at the crack tip by both Irwin and Orowan [18, 19]:

$$\sigma_c = \sqrt{\frac{2E(\gamma_s + \gamma_p)}{\pi a}} \qquad \textbf{(2.3)}$$

where E is the elastic modulus of the material, γ_s is the surface energy of the material, γ_p is the plastic deformation energy, and a is the crack length. The numerator is effectively a material property, and can be replaced with a defined parameter, termed either the critical stress intensity factor, K_c to serve as a scaling factor to define the magnitude of the stress field around the crack tip, or the strain energy release rate, G_c to define the crack driving force [20]:

$$\sigma_c = \frac{K_c}{\sqrt{\pi a}} = \sqrt{\frac{EG_c}{\pi a}} \qquad \textbf{(2.4)}$$

This equation exhibits the interrelation between the three main factors to any fracture process: the stress level, a material parameter (K or G), and the size of the flaw. More specifically, the

stress distribution near the tip of the crack (outside of the small plastic deformation zone) can be represented by the following [21-24]:

$$\sigma_{ij} = \frac{K_I}{\sqrt{2\pi r}}\sigma_{ij}^{I}(\theta) + \frac{K_{II}}{\sqrt{2\pi r}}\sigma_{ij}^{II}(\theta) \qquad \textbf{(2.5)}$$

where $i, j = r, \theta$ respectively and refer to a polar coordinate system defined at the crack tip (see Figure 2.2), K is the stress intensity factor, $\sigma_{ij}(\theta)$ is the angular distribution of stresses around the crack tip, and I and II represent mode I (normal traction) and II (shear traction) loading conditions respectively. The square root of the denominator arises from the strength of the singular nature of the crack tip – the stress level is asymptotic as the distance from the crack tip decreases, with an $r^{-1/2}$ dependency. As seen in equation (2.4), the stress intensity and the energy release rate are interrelated, as shown in Irwin's relation [20]:

$$G = \frac{\left(K_I^2 + K_{II}^2\right)}{\bar{E}} \qquad \textbf{(2.6)}$$

where $\bar{E} = E/1-\nu^2$ in plane strain and $\bar{E} = E$ in plane stress (E is the elastic modulus). Propagation of the crack is expected to occur when either the stress intensity factor or the strain energy release rate reach a critical value.

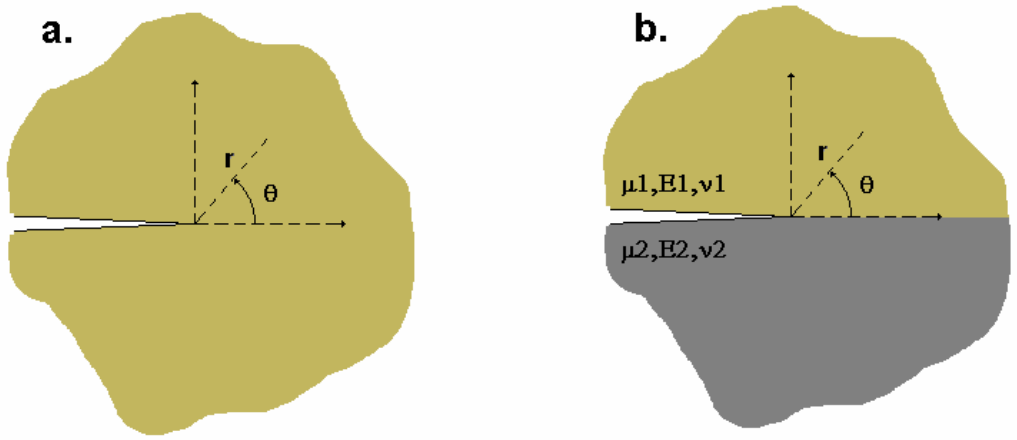

Figure 2.2: Geometry and conventions for a) a bulk crack and b) an interface crack.

As originally proposed by Irwin and Orowan in equation (2.3), and still in the context of linear elastic fracture mechanics, small amounts of plastic deformation at the tip of the crack have a significant impact on the critical stresses and energy for fracture. Although the elastic stress field of equation (2.5) exhibits asymptotic behavior, mathematically resulting in infinite stresses at a short distance from the crack tip singularity, realistically at some distance r the elastic stress will exceed the material yield strength and truncate the stress level at that value [25] (see Figure 2.3). By letting the critical elastic stress in equation (2.5) be equal to the yield stress

(σ_{ys}) at the boundary between the elastic and plastic regions, the equation can be rearranged to estimate the distance r from the crack tip that yielding occurs:

$$r = r_y = \frac{1}{2\pi}\left(\frac{K^2}{\sigma_{ys}}\right) \qquad \textbf{(2.7)}$$

This is effectively a first-order approximation, since there is no reason to assume that the plastic zone is circular, and in actuality the size of the plastic zone varies with θ (recall Figure 2.2), and depends on the whether the stress condition is of plane stress or strain. For cases of plane strain, the triaxial stress field suppresses the plastic zone size, which has been estimated to be a third of that reported in equation (2.7) [26]. Given that there is a high hydrostatic pressure at the crack tip, a better approximation would use the crack-tip stress field to determine the variation of the von Mises stress with distance and angle and set that equal to the yield strength.

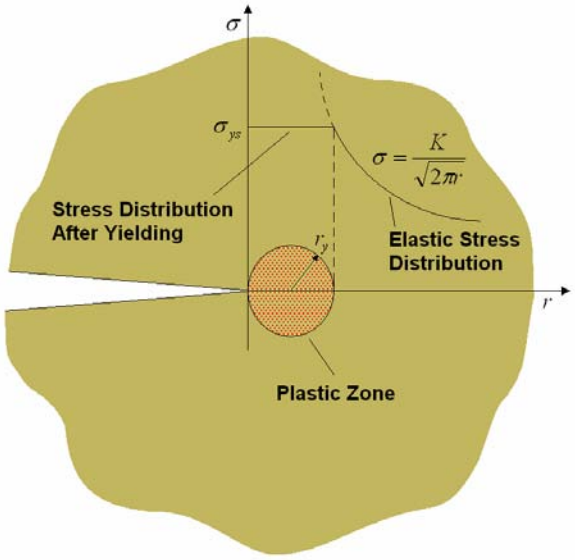

Figure 2.3: Estimation of plastic deformation at a crack tip singularity.

The problem of an interfacial crack between two isotropic linear elastic solids has been examined extensively in the literature, and is well outlined in reviews by Rice [27] and Hutchinson and Suo [28]. The asymptotic stress distribution varies from that of a bulk crack in that the stress state can oscillate near the crack tip, such that the ratio of shear to normal stress varies with distance from the tip of the crack. This arises from the elastic moduli mismatch between the two adjoining materials, which results in a complex stress intensity factor with real and imaginary parts [29]. The Dundur's' elastic mismatch parameters, α and β, are nondimensional terms that measure the mismatch in elastic modulus normal to the interfacial plane and the mismatch in the in-plane bulk modulus respectively [30]:

$$\alpha = (\bar{E}_1 - \bar{E}_2)/(\bar{E}_1 + \bar{E}_2)$$
$$\beta = \frac{1}{2}\frac{\mu_1(1-2\nu_2) - \mu_2(1-2\nu_1)}{\mu_1(1-\nu_2) - \mu_2(1-\nu_1)} \qquad \textbf{(2.8)}$$

where μ_i is the shear modulus, and ν_i is Poisson's ratio of the respective materials (i = *1, 2*). The Dundurs' parameters usually fall in the ranges: $1 \leq \alpha \leq -1$ and $0 \leq \beta \leq \alpha/4$, where interchanging the materials reverses the sign of the parameters and for no material mismatch: $\alpha = \beta = 0$ [31]. Alternatively then, the interfacial crack tip stress field has the general form [32-34]:

$$\sigma_{\alpha\beta} = \frac{\mathrm{Re}[Kr^{i\varepsilon}]}{\sqrt{2\pi r}}\sigma^{I}_{\alpha\beta}(\theta,\varepsilon) + \mathrm{Im}\frac{[Kr^{i\varepsilon}]}{\sqrt{2\pi r}}\sigma^{II}_{\alpha\beta}(\theta,\varepsilon) \qquad \textbf{(2.9)}$$

where $K = K_1 + iK_2$ and is defined as the complex stress intensity factor for an oscillating crack singularity with real K_1 and imaginary K_2 parts. These terms play roles similar to conventional mode I and II intensity factors, though they are coupled and cannot be determined independently of one another as with the bulk crack. The oscillatory stress behavior arises from the $r^{i\varepsilon}$ term, which depends on the oscillatory index [5]:

$$\varepsilon = \frac{1}{2\pi}\ln\left(\frac{(1-\beta)}{(1+\beta)}\right) \qquad \textbf{(2.10)}$$

For $\varepsilon = 0$ (i.e. $\beta = 0$), the tractions ahead of the crack tip represent the normal and shear interpretations of equation (2.15). Suo and Hutchinson [35] and Rice [27] make a case for ignoring ε–effects, however for an underfill/silicon interface, the elastic mismatch between the two (α = 0.80-0.85 and β = 0.19-0.23) is somewhat compelling to consider the oscillatory behavior.

Similar to that for a bulk crack, the energy release rate for crack advance at an interface is related to the stress intensity factors [33, 36]:

$$G = \frac{(1-\beta^2)}{E_*}\left(K_1^2 + K_2^2\right) \qquad \textbf{(2.11)}$$

where $1/E_* = 1/2\left((1-\nu_1^2)/E_1 + (1-\nu_2^2)/E_2\right)$ for plane strain and $1/E_* = 1/2\left(1/E_1 + 1/E_2\right)$ for plane stress. While the complex stress intensity solutions for interfacial cracks exist in the literature, it is often more convenient to express the interfacial fracture toughness in terms of the strain energy release rate, as it offers the advantages of being easy to compute and is invariant with respect to the position of the interfacial crack (i.e. at the interface, near the interface, etc.) [37]. However, the strain energy release rate has a strong dependence on the mix of in-plane shear (mode II) and normal (mode I) tractions at the crack tip and when reported, should be accompanied by a mode-mix phase angle for the particular test geometry:

$$\psi = \tan^{-1}\left[\frac{\mathrm{Im}\left(Kl^{i\varepsilon}\right)}{\mathrm{Re}\left(Kl^{i\varepsilon}\right)}\right] \quad \textbf{where} \quad \psi = \tan^{-1}\left[\frac{K_2}{K_1}\right] \quad \textbf{when } \boldsymbol{\varepsilon = 0}. \quad \textbf{(2.12)}$$

The term l is a reference length with respect to the crack tip, a required specification, since when $\varepsilon \neq 0$ the ratio of shear traction to normal traction varies at distances of typical interest from the crack tip. The selection is arbitrary and so long as the value is reported, the mixity can be calculated for any fixed length [38]:

$$\psi_2 = \psi_1 + \varepsilon \ln\left(\frac{l_2}{l_1}\right) \qquad \textbf{(2.13)}$$

Interfacial fracture mechanics has been applied to several sandwich geometries to characterize the critical strain energy release rate of underfill interfaces. Among others, Wang and Suo [39] have measured interfacial fracture toughness for a range of phase angles using a brazil nut specimen, Liechti and Chai [40] have used a bimaterial beam geometry, Lui *et al.* [41] have measured the effect of mixity using an edge notch flexure specimen, while others have measured strain energy release rates for geometries more applicable to a microelectronics assembly, such as Charalambides *et al.* [42] using a notched four-point bend specimen and Yan and Agarwal [38] using a flip-chip four-point bend specimen (see Figure 2.4). Historically, one of the most popular methods to measure critical strain energy release rates is through the use of a double cantilever beam geometry. It can be shown that for an elastic body, the strain energy release rate is related to the compliance (displacement/load) [43]:

$$G = \frac{P^2}{2w}\left(\frac{dC(a)}{da}\right) \qquad \textbf{(2.14)}$$

where P is the applied load, w is the width, a is the crack length, and $C(a)$ is the compliance, which is a cubic function of crack length. Using simple beam theory, the compliance of a symmetric double cantilever beam may be expressed as:

$$C(a) = \frac{8a^3}{Ewh^3} \quad \text{where} \quad \frac{dC(a)}{da} = \frac{24a^2}{Ewh^3} \qquad \textbf{(2.15)}$$

where E is the elastic modulus of the double cantilever beam adherends, and $2h$ is the height of the double cantilever beam. The resulting strain energy release rate is then:

$$G = \frac{12P^2a^2}{Ew^2h^3} \qquad \textbf{(2.16)}$$

This equation allows for the critical energy release rate to be determined for crack propagation at a particular bimaterial interface from the critical applied load and the compliance of the specimen (measure of the inverse slope of the load-displacement curve), which can be used to solve for the crack length. This analysis is very simplified, and is based on the assumption that the compliance at the crack tip is zero. In practice, due to a finite crack length, rotation and deflection of the beams occur, and requires modification of the strain energy release rate equation [44].

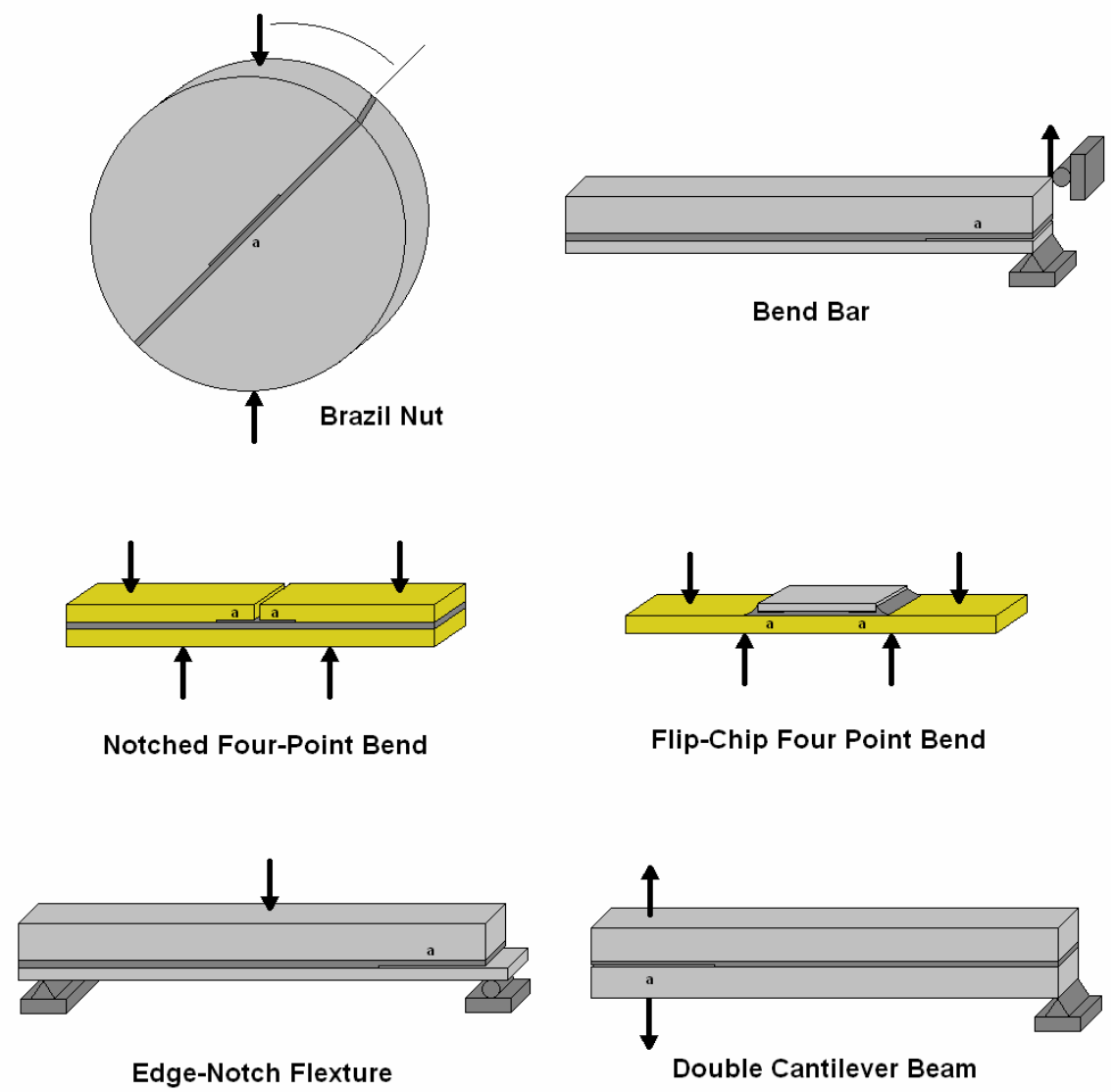

Figure 2.4: Geometries of typical adhesion test specimens.

2.3 Interfacial Stress Singularity Mechanics

Understanding the initiation stage of interfacial crack formation has become increasingly important under the current trend to decrease package feature sizes. However, in the absence of an interfacial crack, the traditional fracture mechanics analyses which are applied to the aforementioned tests no longer apply. Fracture mechanics provides a specific solution for a sharp crack singularity, however interfacial failure can initiate at other interfacial singularities such as edges and corners prior to crack formation. Looking at an interfacial crack as a bimaterial wedge with angles $\alpha_1 = \pi$ and $\alpha_2 = -\pi$, a similar approach can be taken for singularities where α_1 and α_2 are more generalized (see Figure 2.5) [45].

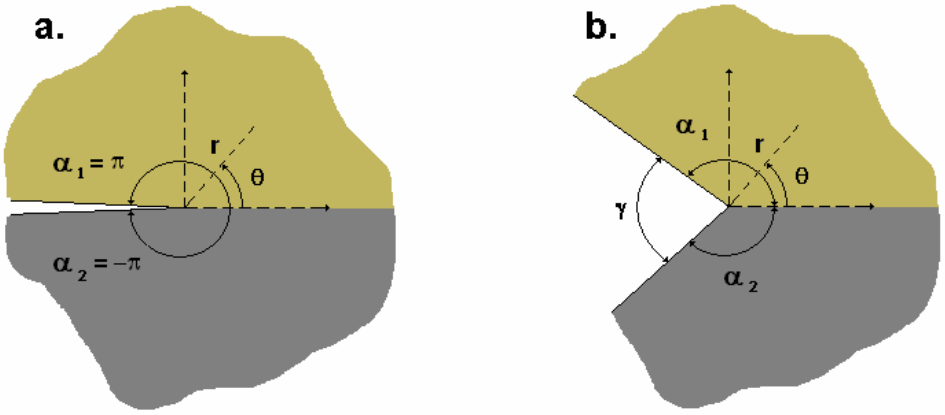

Figure 2.5: Polar coordinate system for a) a sharp crack bimaterial wedge and b) a generalized bimaterial wedge.

For two isotropic elastic solids joined at an interface, the singularity region looks asymptotically like two bonded wedges. The stress state near the apex of dissimilar bonded wedges for plane stress or strain has the form [45-49]:

$$\sigma_{ij} = \sum_{n=1}^{N} K_{an} r^{\lambda_n - 1} \overline{\sigma}_{ijn}(\theta) + K_{a0} \overline{\sigma}_{ij0}(\theta) \qquad \textbf{(2.17)}$$

where i,j = r,θ respectively and refer to a polar coordinate system defined at the interface corner (see Figure 2.5). One or more singularities can exist for certain geometries, and the order of the singularities, the stress intensity factors, and the angular distributions generally are complex due to the elastic mismatch described by the Dundurs' parameters. As with the interfacial crack problem, in the absence of a mismatch, the stress is nonoscillating and these terms are real. The number of singular terms (N), as well as the strength (λ_n-1) and angular variation ($\overline{\sigma}(\theta)$) of the singularities are determined through asymptotic analysis using non-dimensional elastic properties, local geometry, and boundary conditions. The K_{an} ('a' subscript corresponds to apex of a wedge) stress intensity factors will determine the individual contribution of each singular term in the series, similar to the stress intensities for a crack singularity, and depend on the elastic properties, global geometry, and applied loads [50, 51]. The r-independent $K_{a0}\overline{\sigma}_{ij0}(\theta)$ term exists mainly for interfaces subjected to thermally induced strains or locally applied loads. For global loads applied to the bonded joint, the term usually vanishes [52-54]. Similar to the asymptotic behavior of a crack tip (λ-1 = -0.5), the stress level of the singularity approaches infinity for a decreasing distance, with an $r^{\lambda-1}$ dependency (Figure 2.6). The more severe the singularity, the higher the stress level is for a particular distance.

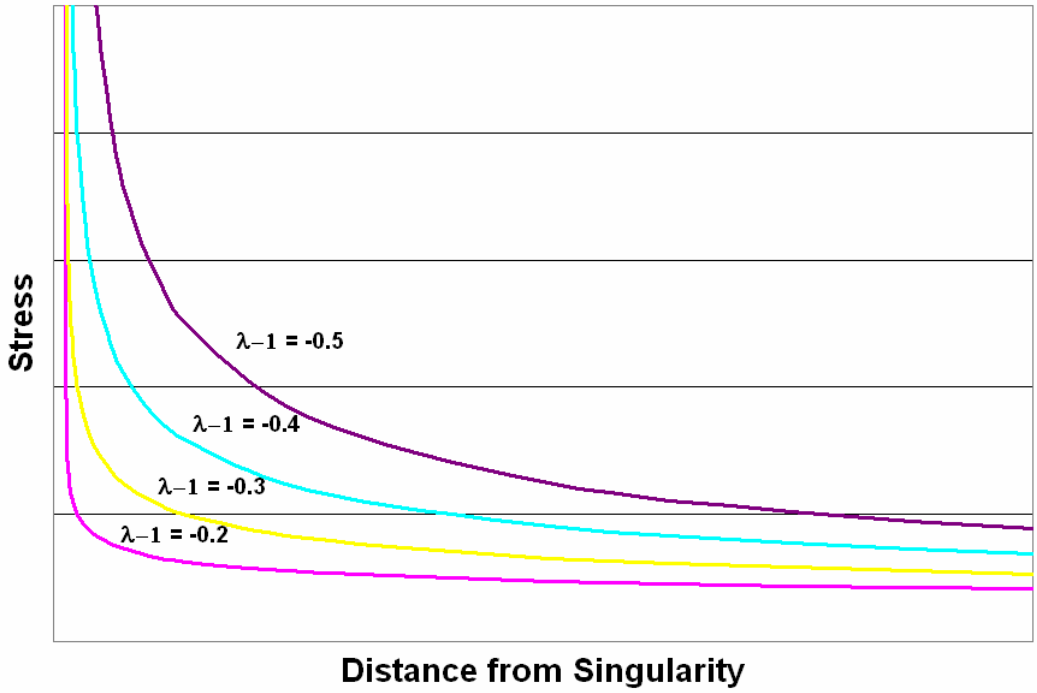

Figure 2.6: Stress versus distance from singularity for various singularity strengths.

Although an accepted methodology to predict initiation has yet to be established, several investigators have proposed predicting failure in uncracked bonded joints using the aforementioned stress singularity approach. Gradin applied this approach to failure of steel/epoxy sandwich specimens subjected to three different loading conditions [47]. In a test of eight samples, the results indicated a relatively constant value of the stress intensity factor, with only one outlying data point. In another investigation, Groth correlate finite element predictions with experimental results of lap shear joints containing a spew fillet at several overlap lengths [55]. The embedded corner of the joint was described by two real singularities and used to generate an equivalent generalized stress intensity factor that exhibited good predictive capability for large overlap lengths. At small lengths, the agreement between the test results and predictions were poor, which was explained by the author as possibly being affected by non-linear material behavior or an imperfect sharpness to the embedded corner. In a study applying the stress singularity approach to microelectronics packaging, Hattori *et al.* investigated cooling-induced delaminations of packaged iron-nickle sheets, with applications to microelectronic packages [56, 57]. The samples had different geometries and thus each exhibited a different singularity strength, so the authors developed a relation between the stress intensity factor and the order of the singularity. This correlation was used to predict delamination, which was consistent with the test results.

More recently, Reedy has composed a significant body of work applying the stress singularity approach to an adhesively bonded butt joint geometry [53, 54, 58-66]. This work

included testing a significant number of both aluminum and steel adherends bonded together by an unfilled epoxy adhesive. The studies included the effect of bondline thickness, the effect of adherend stiffness, plasticity effects, the effect of residual stress and stress relaxation, the effect of surface preparation, and the correlation with interfacial fracture mechanics. In two reported studies on the effect of bondline thickness, one with steel adherends [62] and one with aluminum adherends [65], the testing reveled that the critical stress intensity factor remained relatively constant with varying bond thickness, indicating that the value was a material property that could be used to predict failure. The investigation of the aluminum adherend joints also showed that the reduction of the modulus from steel to aluminum resulted in a decrease of the stress singularity, with the same predictive capability. Testing for the effect of residual stress and stress relaxation seemed to indicate that residual stresses generated during sample cool-down after cure had little effect on joint strength. Compression tests of the bulk epoxy showed that significant stress relaxation could occur for stress levels that approached the epoxy yield strength, and it was suggested that stress relaxation might occur at the interface free-edge [53]. The results did indicate that in most cases of practical interest, both the residual stress and stress relaxation could be ignored. A later study on surface preparation revealed that the critical stress intensity factors were strongly dependent on surface roughness, with only a modest effect of method of cleaning [66].

2.4 Objective

The objective of this research was to examine the correlation between interfacial strengths measured in terms of different geometric singularities. Standard interfacial fracture mechanics testing will be performed using an asymmetric double cantilever beam geometry (ADCB), while the stress singularity criterion will be applied to a tensile butt joint geometry (TBJ). Additionally, modified tensile butt joint geometries will be used to examine the effect of geometric discontinuity on joint strength. The following will discuss our work on examining adhesive strength for underfill/polyimide interfaces found in microelectronic assemblies and moreover, the effect of changing the dominating singularity in the TBJ specimens to mimic other geometric discontinuities found in the assembly.

CHAPTER 3 – EXPERIMENTAL APPROACH

3.1 Materials

The underfill resins studied in this investigation included a bisphenol A/amine curing agent system, a bisphenol F resin/2,4-EMI curing agent system and a cycloaliphatic resin/anhydride curing agent system, as well as three commercial underfill resins: Zymet X6-82-5LV, Dexter FP-4531, and Loctite 3563. Two passivations were used for this study: HD Microsystems' PI-2555 (a commercially available BTDA-ODA-MPDA polyimide) and a model coating consisting of a mixed organosilane monolayer (1-bromo-11-undecyltrichlorosilane and dodecyltrichlorosilane).

3.2 Adhesion Test Sample Preparation

3.2.1 Asymmetric Double Cantilever Beam Specimens

ADCB test specimens were prepared based on modifications of procedures developed at Sandia National Laboratories [67]. For an asymmetric geometry, the adherends are machined as two beams of different thicknesses, as can be seen in Figure 3.1. The top beam is machined to dimensions: 9.5 x 12.7 x 123.2mm. Holes of 3.2mm diameter are drilled through the front and back ends of the beam for underfill flow. A 3.2mm hole is drilled 7.9mm from the front end, centered in the height of the beam for the loading pin. The bottom beam is machined to dimensions: 4.7 x 12.7 x 123.2mm. A hole of 3.2mm diameter is drilled 7.9mm from the front end of the beam, centered in the height of the beam for the other loading pin.

Figure 3.1: Prepared ADCB specimen.

ADCB specimens with both aluminum/underfill and polyimide/underfill interfaces were prepared for the three model unfilled, three model filled and the three commercial systems. To prepare the samples, the aluminum adherends were first ground and polished to obtain a 10nm RMS surface polish (as measured through atomic force microscopy). Care was taken to ensure that the edges were kept sharp and unbroken. The surfaces were cleaned, and for the passivated samples, polyimide was spin-coated and cured on the aluminum surface to create a 15um thick layer. To create a precrack region for the test, the first 25.4 mm of the thinner beams were sputtered with a thin layer of gold-paladium.

A 250μm thick piece of shim stock was cut and adhered with a small amount of superglue to the thicker beam on the front two corners and across the back side to provide the gapping for the underfill bondline. The beams were then heated to 80°C to ensure the superglue completely cured. With the prepared surfaces facing in, the two beams were sandwiched and

held together with polyimide tape, completely sealing the bondline gap. The samples were placed in a Blue M circulating oven at 80°C for 1 hour to allow for better underfill flow. Underfill was force-flowed from the front hole until a small amount of underfill began to rise out of the evacuation hole. The specimens were cured according to the recommended cure schedules. A schematic of the sample procedure can be seen in Figure 3.2.

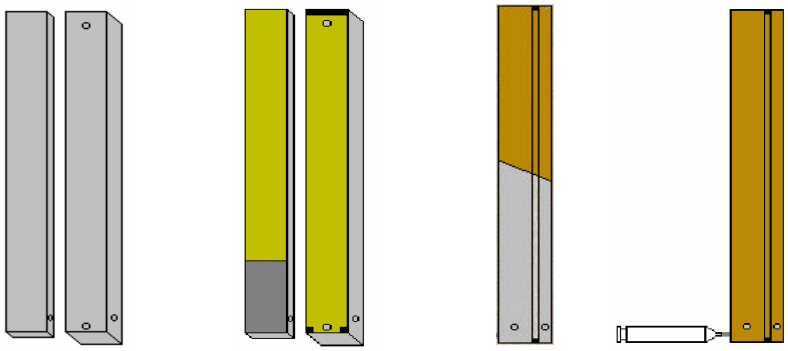

Figure 3.2: ADCB sample preparation procedure.

3.2.2 Tensile Butt Joint Specimens

For the TBJ specimens, four different modifications of the tensile joint geometry were chosen: free-edge (TBJ-FE), free-corner (TBJ-FC), embedded-edge (TBJ-EE), and embedded-corner (TBJ-EC) singularity geometries, based on those found in a flip-chip geometry (see Figure 3.3). For the free-edge TBJ test, the two cylinders are identical; machined to a 28.6 mm diameter and a 38.1mm length. A 12.7mm hole is tapped in the center of the back side with 13-thread and a depth of 12.7mm for mounting the sample into the testing load chain. The cylinders are very carefully machined: the front and back surfaces have a parallel tolerance of 0.0127mm and the side has a perpendicular tolerance of 0.0711mm to the front and back surfaces. For the free-corner TBJ test, the cross sectional area was kept the same as the round specimen, with dimensions 25.4 x 25.4mm. The lengths and tolerances are the same as for the round specimens, with extreme care taken to keep the corners very sharp. Holes are tapped in the backs of the specimens to the same specifications as the round samples. The large cylindrical bases for the embedded TBJ tests have diameters of 50.8mm and the same lengths and loading holes as the other specimens.

As with the ADCB specimens, the free-edge TBJs were prepared with all nine underfill materials, bonded to both bare aluminum and polyimide-coated surfaces. Additionally, a set of free-edge TBJ samples was prepared with mixed organosilane monolayer-coated surfaces and bonded with the bisphenol A/T-403 underfill. The other three TBJ geometries were only tested with the 3 commercial underfills, bonded to polyimide-coated adherends. The adherends were all polished, cleaned and polyimide-coated (if necessary) with procedures identical to the ADCB specimens, with extreme care to keep the edges and corners sharp and unbroken. For the TBJ samples requiring the self-assembled monolayer coating, organosilane solutions with increasing bromine content were heated to 60°C in a nitrogen-purged glove box and the cleaned/polished

adherends were submerged and covered for 5 hours. After deposition, the adherends were removed and cleaned ultrasonically in both toluene and acetone for 30 minutes each.

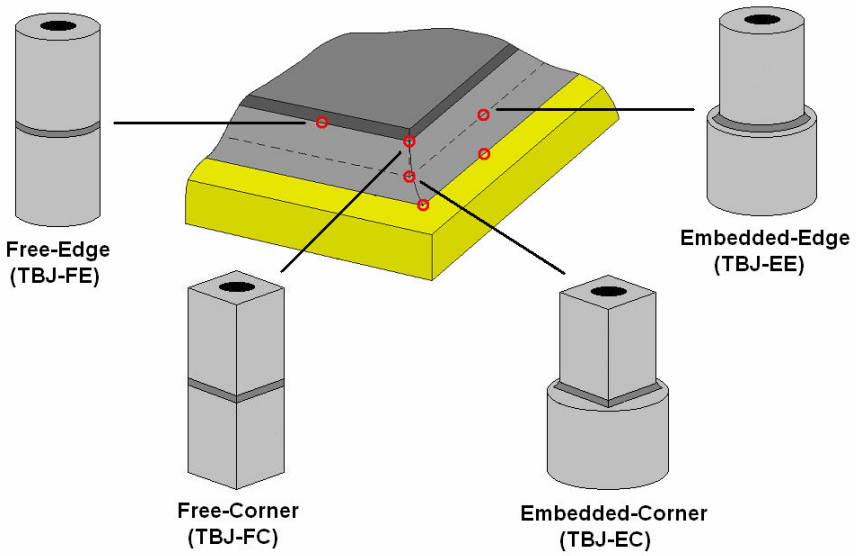

Figure 3.3: Four types of TBJ geometries studied.

Tensile butt joint assembly and alignment was achieved using two L. S. Starrett precision V-block and clamp sets mounted to a locking base. For the free-edge and free-corner TBJ specimens, the two adherends were placed on each of the two v-blocks, with the prepared surfaces facing in. Gapping between the two was achieved with the 250μm shim stock, with the samples clamped into place and the shim removed. The gap was sealed with polyimide tape, leaving two holes 180° apart for underfill flow and evacuation at the bondline. Both round and square collars were obtained from McMaster-Carr and tapped with two holes on opposite sides to line up with the holes in the polyimide tape. The collars were clamped around the taped bondline, silicone o-rings were placed in the collar holes, and nylon tube-to-pipe adapters were threaded into the holes to form a tight seal with the sides of the TBJ specimen. The samples could then be removed from the V-blocks and short lengths of 1/4”OD, 1/8”ID Tygon tubing was fitted onto the barbed ends of the adapters to act as reservoirs for excess underfill. The samples were placed in a circulating oven to equilibrate at 80°C, and syringes of the underfill were fitted onto one side of the tubing. Underfill was force-flowed through the specimen until no air bubbles exited out of the evacuation hole. Samples were cured vertically See Figure 3.4 for images of the sample fixturing.

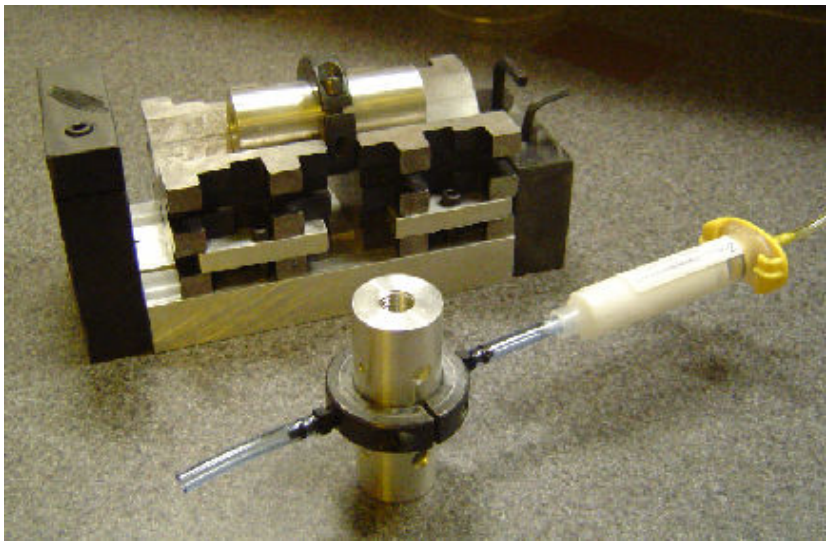

Figure 3.4: TBJ-FE sample preparation procedure (TBJ-FC preparation uses square collar).

For the two embedded-type specimens, a spacer was placed on one of the V-blocks to align the smaller round or square adherend with the center of the larger round adherends. As with the free-edge and free-corner samples, the gapping was set with the shim stock, the samples were locked into place with the clamps and the spacer was removed (see Figure 3.5). The V-block setups were placed in a circulating oven to equilibrate at 80°C, aligned vertically with the larger round cylinder on the bottom. Using a 20 gauge (0.61mm ID) diameter needle, underfill was auto-dispensed along half of the perimeter to fill the gap between the two adherends. Care was taken to be consistent with the fillet at the edges. The V-block setups were cured vertically.

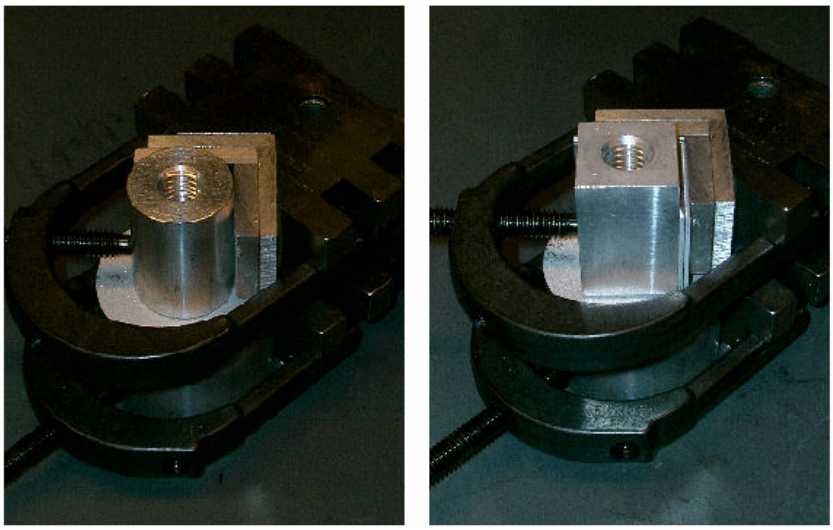

Figure 3.5: TBJ-EE and TBJ-EC specimen setup.

3.3 Monotonic Interfacial Fracture Testing

3.3.1 Asymmetric Double Cantilever Beam Testing

The ADCB specimens were loaded in monotonic tension on the Instron 5567 under displacement control at a crosshead rate of 1.27mm/min. For this test, elastic strain energy is stored in the aluminum adherends until sufficient energy can be released to propagate the interfacial crack. After a critical load level is reached for that particular crack length, the crack begins to advance and the load and subsequent strain energy drop as the energy goes to create the new delaminated surfaces. The crosshead is reversed to unload the specimen, and the test is repeated again at the new crack length. For each loading and unloading cycle, the compliance of the specimen can be used to infer a crack length. This process was repeated 5-7 times to give measurements for several different interfacial crack lengths (see Figure 3.6). In order to use crosshead displacement for the compliance measurement, the stiffness of the load train was determined using a high modulus steel sample. Reported displacements are crosshead measurements that have been corrected to remove the compliance of the fixturing.

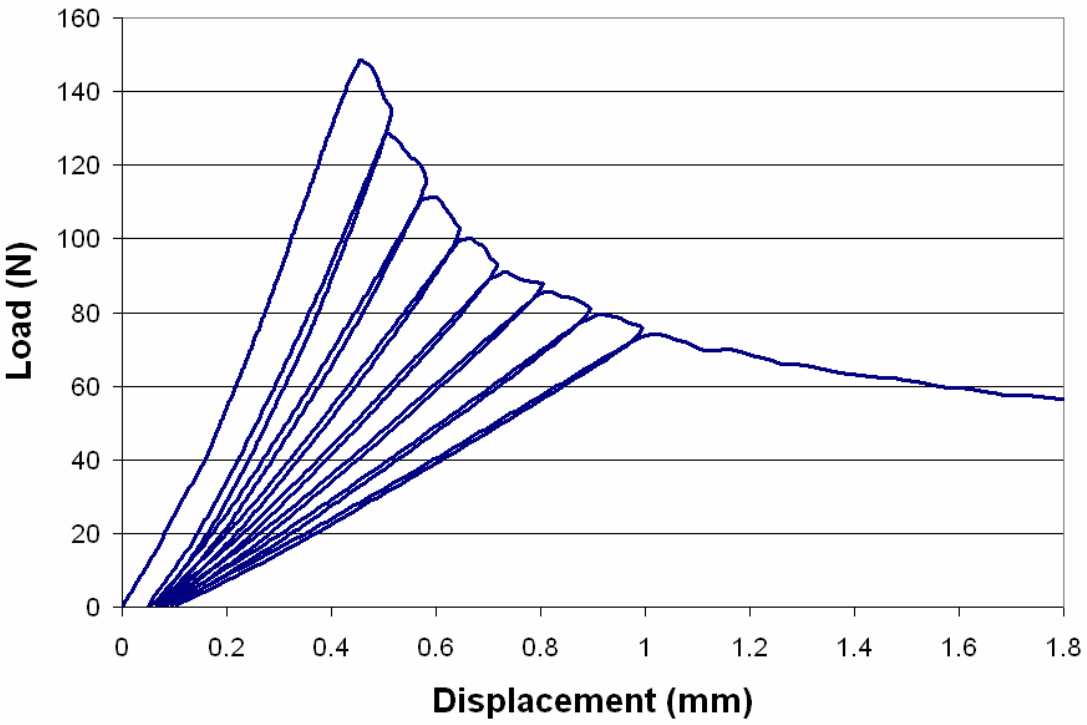

Figure 3.6: Typical load vs. displacement curve for the static ADCB test.

A specimen calibration developed by Bao *et al.* for the interface crack stress field was used to calculate the critical strain energy release rate for the various crack lengths. This calibration can be applied to a sandwich specimen when the bond is suitably thin [68]:

$$G_{DTC} = \frac{6(Pa)^2(1+\eta^3)}{E_1' h^3 w^2}\left[1+0.677B(\eta)\frac{h}{a}\right]^2 \qquad \textbf{(3.1)}$$

where P is the maximum load, a is the crack length measured from the loading axis, E_1' is the elastic modulus of the aluminum adherend, η is the ratio of heights of the thinner beam to thicker beam, h is the height of the thinner beam, and $B(\eta) = 1.120 - 0.695(\eta - 0.585)^2$. For an epoxy bonded between two aluminum adherends, the mode mixity for this ADCB geometry has been determined by Reedy *et al.* to be -8° for a distance 0.01mm ahead of the crack tip [67]. The DTC subscript refers to the critical (C) failure at an interfacial disbond tip (DT), and was established to differentiate between the critical stress intensity factors determined from the above energy release rates and the critical stress intensity factor for the TBJ test.

The crack length was measured from beam compliance, as the inverse slope of the loading curves from the ADCB load and displacement data. The compliance equation can be determined from Equation (3.1) from the relation shown in Equation (2.14):

$$C = \frac{4a^3(1+\eta^3)}{E_1' h^3 w}\left[1+3\left(Y_I'(\rho')B(\eta)\frac{h}{a}\right)+3\left(Y_I'(\rho')B(\eta)\frac{h}{a}\right)^2\right] \qquad \textbf{(3.2)}$$

Solving this cubic equation using Cardano's methodology and taking the real root, the crack length for a particular beam compliance can be calculated [69].

3.3.2 Tensile Butt Joint Testing

The butt joint specimens were loaded under monotonic tension on a screw-driven Instron 4206 materials testing machine under displacement control at a crosshead rate of 1.27mm/min. Samples were loaded until catastrophic failure of the entire joint (see Figure 3.7). For the free-corner, embedded-edge, and embedded-corner specimens, no specimen calibrations for the stress intensity factors are available, and characterization was limited to measurement of the ultimate joint strength. Specimen calibrations for the free-edge samples are available and were used to determine critical stress intensity factors for comparison with the ADCB results.

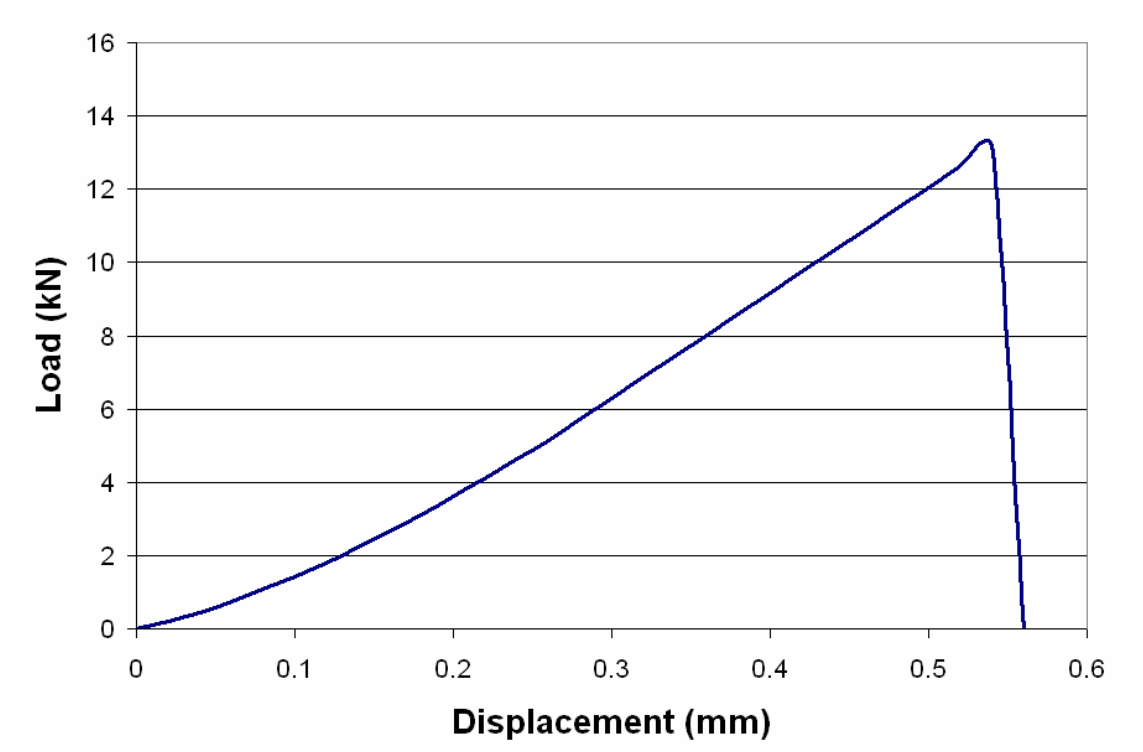

Figure 3.7: Typical load vs. displacement curve for the static TBJ test.

Reedy [52-54] has developed a stress intensity factor relationship for an interface corner (stress-free edge) in a tensile butt joint (TBJ). The characteristic length scale is the half-bond thickness (see Figure 3.8). The measured ultimate tensile stress (σ_{ult}) of the joint is used to calculate the characteristic in-plane stress (σ^*), remote from the stress-free edge [54]:

$$\sigma^* = \left(\frac{\nu_2}{1-\nu_2}\right)\left[1-\left(\frac{E_2}{E_1}\frac{\nu_1(1+\nu_1)}{\nu_2(1+\nu_2)}\right)\right]\sigma_{ult} \qquad \textbf{(3.3)}$$

where v_i is Poisson's ratio and E_i is Young's Modulus for the aluminum (1) and the underfill resin (2). The characteristic stress, σ^*, is used to calculate the critical interfacial free-edge (FEC) stress intensity factor for the joint:

$$K_{FEC} = \sigma^* h^{1-\lambda} A_p(\alpha,\beta) \qquad \textbf{(3.4)}$$

where h is the half thickness of the underfill layer, $1-\lambda$ is the negative of the order of the stress singularity, and $A_p(\alpha,\beta)$ is a non-dimensional function involving the elastic mismatch parameters at the interface defined in equation (2.20) [54]. For the case of an epoxy adhesive bonded between two aluminum adherends under tensile loading, Reedy has calculated $1-\lambda$ as 0.268 and $A_p(\alpha,\beta)$ as 1.061 [52].

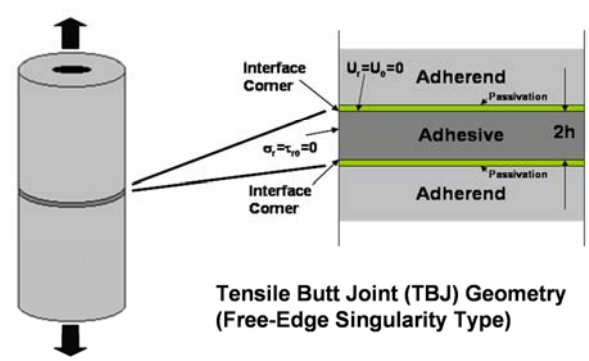

Figure 3.8: Schematic diagram of the asymptotic problem for a modified tensile butt joint.

3.4 Tensile Butt Joint Fatigue Testing

Mechanical fatigue of the TBJ-FE geometry was applied by a servo-hydraulic MTS materials testing machine using a max/min load ratio of 0.1 and a frequency of 10 Hz (see Figure 3.9). Using the monotonically loaded TBJ strengths as a reference, the TBJ samples were tested in batches of five at several sub-critical (relative to the monotonically loaded TBJ) load levels to determine the fatigue lifetime. It was assumed that catastrophic failure occurred immediately at initiation, so joint failures were assumed as initiation lifetimes.

Figure 3.9: Tensile butt joint fatigue setup.

CHAPTER 4 – RESULTS AND DISCUSSION

4.1 Interfacial Fracture Toughness

4.1.1 ADCB Testing

Critical energy release rates were measured for the three model and three commercial underfill systems bonded to both aluminum and polyimide-coated aluminum surfaces. The values were converted to critical stress intensities using equation (2.11) and the visual failure modes were recorded for all of the tests. The experimental results can be seen in Table 4.1.

Table 4.1: Adhesion results on underfill/aluminum and underfill/passivation interfaces.

Surface	6061-T6 Aluminum			PI-2555 Polyimide		
Underfill	G_{DTC} (J/m^2)	$\|K_{DTC}\|$ ($MPa\text{-}m^{1/2}$)	Visual Failure	G_{DTC} (J/m^2)	$\|K_{DTC}\|$ ($MPa\text{-}m^{1/2}$)	Visual Failure
Bis. A/T-403 (Unfilled)	170.1 ±7.8	0.94 ± 0.02	Coh.	152.1 ± 6.2	0.89 ± 0.02	Coh.
Bis. A/T-403 (Filled)	198.9 ±10.4	1.44 ± 0.04	Coh.	175.9 ± 5.0	1.35 ± 0.02	Coh.
Bis. F/2,4-EMI (Unfilled)	38.2 ± 4.9	0.49 ± 0.03	Adh.	27.9 ± 2.8	0.42 ± 0.02	Adh.
Bis. F/2,4-EMI (Filled)	49.1 ± 3.4	0.73 ± 0.03	Adh.	35.2 ± 2.9	0.61 ± 0.03	Adh.
Cyclo./Anh. (Unfilled)	43.6 ± 7.5	0.51 ± 0.04	Adh.	24.2 ± 2.5	0.38 ± 0.02	Adh.
Cyclo./Anh. (Filled)	36.2 ± 5.7	0.62 ± 0.05	Adh.	20.9 ± 4.2	0.47 ± 0.05	Adh.
Dexter FP-4531	29.4 ± 2.9	0.70 ± 0.03	Adh.	28.1 ± 2.9	0.69 ± 0.04	Adh.
Loctite 3563	98.1 ± 4.3	1.04 ± 0.02	Coh.	91.4 ± 2.3	1.01 ± 0.01	Coh.
Zymet X6-82-5LV	122.7 ± 7.5	1.58 ± 0.05	Coh.	110.0 ± 3.5	1.50 ± 0.02	Coh.

Between the two substrates, the critical strain energy release rates were higher for the aluminum surface than they were for the polyimide, ranging from a factor of 1.04 to 1.80. This higher adhesion is expected, given that polyimide typically exhibits a lower surface energy than the native oxide on the surface of aluminum. A total solid surface energy of approximately 40 mJ/m^2 has been measured for polyimide [70], while aluminum oxide has range of values reported throughout the literature, ranging anywhere from 40 to 638 mJ/m^2, depending on the surface preparation [71, 72]. Luo and Wong report that the dispersive surface energy of UV/ozone-cleaned alumina is 45.9 mJ/m^2 [73]. Although they were unable to provide the non-dispersive component, they do report a total surface energy of the aluminum oxide before cleaning as 39.1, with a dispersive contribution of 37.0. Assuming that the total surface energy of the aluminum oxide could fall between 50-55 mJ/m^2 with the non-dispersive component contribution, the value is approximately 1.2-1.3 times larger than the reported polyimide value.

Interestingly, this is well within the range of the factors seen for the ADCB testing. Given the sensitivity of the aluminum to surface treatment, the variability of adhesion strengths between the polyimide and aluminum seems reasonable.

Similar trends were observed for both the aluminum and polyimide surfaces. The bisphenol A/T-403 underfill exhibited the highest adhesion of all of the materials, while the Loctite and Zymet underfills exhibited similarly high interfacial fracture toughness values. The bisphenol F, cycloaliphatic, and Dexter materials exhibited much lower toughness values. The addition of filler to the two bisphenol model materials resulted in an increase in the interfacial fracture toughness. The addition of filler results in an increased energy dissipation in the underfill, which adsorbs energy that would otherwise go to separating the interface. Alternatively, the cycloaliphatic model system exhibited a decrease in toughness with the addition of filler. The energy dissipation mechanism from the filler does not operate at the interface, and the presence of the filler results in a decrease in the plastic deformation at the interfacial crack tip.

4.1.1.1 Locus of Failure

Scanning electron microscopy (SEM) and x-ray photoemission spectroscopy (XPS) were performed on the fracture surfaces to provide more insight into the failure mechanisms in the ADCB tests. For the cohesive failures, fracture surfaces were examined for similarities to the bulk fracture under SEM, while XPS was used to confirm the location of the interfacial crack path (adhesive vs. cohesive failure) for the visually-determined adhesive ADCB failures.

The results of the XPS can be seen in

Table 4.2. The values in the table are ratios of the respective peak heights to that of the carbon peak. Examination of the polyimide fracture surfaces for all of the underfills shows almost no compositional difference from that of an unbonded polyimide surface. From this, it can be inferred that no epoxy has transferred to the polyimide layer during delamination. The underfill side is more complicated, with differences seen between the bulk and fracture surface silicon and oxygen contents for the filled underfills as well as the bulk and fracture surface nitrogen content for the bisphenol F/2,4-EMI underfills.

The higher silicon and oxygen concentrations in the bulk of the filled systems are expected, as a bulk fracture would expose more of the silica than would be seen at the resin-rich underfill/polyimide interface. The smaller difference between the bulk and fracture surface of the cycloaliphatic material can be explained by the strong bonding between the particles and the matrix; bulk fracture is easier in the matrix than at the underfill/silica interface, resulting in less silica surface exposed than for fracture at the weak underfill/silica interfaces in the Dexter and bisphenol F underfills. The nitrogen concentration difference for the bisphenol F underfills could be attributed to polyimide transfer, however it is possible that the increase in nitrogen is due to a higher concentration of 2,4-EMI at the surface. Due to the strong molecular interactions between the 2,4-EMI and polyimide, it is highly likely that the 2,4-EMI preferentially bonds to the polyimide before underfill cure, causing a off-stoichiometric amount of 2,4-EMI at the interface. This seems to be confirmed by the slight increases in nitrogen content on the polyimide side with the increasing amount of EMI. It is more likely that the higher nitrogen is

caused by additional EMI than a larger amount of polyimide cohesive failure for the small increases in interfacial fracture toughness that was seen. For the Dexter, unfilled cycloaliphatic, and filled cycloaliphatic surfaces, the lack of any nitrogen indicates that no polyimide has been transferred to the underfill, allowing for confirmation that the interfacial failure was adhesive in nature.

Table 4.2: Atomic ratios for the fracture surface compositions.

Underfill	*Surface*	*O/C*	*N/C*	*Si/C*
Bis. F/4 phr 2,4-EMI (Unfilled)	Bulk Epoxy	0.1853	0.0240	0.0000
	Epoxy Fracture Surface	0.1862	0.0255	0.0000
	Unbonded Polyimide	0.1759	0.0664	0.0000
	Polyimide Fracture Surface	0.1751	0.0673	0.0000
Bis. F/6 phr 2,4-EMI (Unfilled)	Bulk Epoxy	0.1843	0.0269	0.0000
	Epoxy Fracture Surface	0.1847	0.0291	0.0000
	Unbonded Polyimide	0.1759	0.0664	0.0000
	Polyimide Fracture Surface	0.1760	0.0666	0.0000
Bis. F/8 phr 2,4-EMI (Unfilled)	Bulk Epoxy	0.1869	0.0286	0.0000
	Epoxy Fracture Surface	0.1835	0.0312	0.0000
	Unbonded Polyimide	0.1759	0.0664	0.0000
	Polyimide Fracture Surface	0.1779	0.0651	0.0000
Bis. F/4 phr 2,4-EMI (Filled)	Bulk Epoxy	0.3346	0.0257	0.0381
	Epoxy Fracture Surface	0.2799	0.0259	0.0069
	Unbonded Polyimide	0.1759	0.0664	0.0000
	Polyimide Fracture Surface	0.1731	0.0670	0.0000
Cyclo./Anhydride (Unfilled)	Bulk Epoxy	0.2566	0.0000	0.0000
	Epoxy Fracture Surface	0.2621	0.0000	0.0000
	Unbonded Polyimide	0.1759	0.0664	0.0000
	Polyimide Fracture Surface	0.1737	0.0676	0.0000
Cyclo./Anhydride (Filled)	Bulk Epoxy	0.2869	0.0000	0.0130
	Epoxy Fracture Surface	0.2607	0.0000	0.0062
	Unbonded Polyimide	0.1759	0.0664	0.0000
	Polyimide Fracture Surface	0.1786	0.0669	0.0000
Dexter FP-4531	Bulk Epoxy	0.3388	0.0000	0.0524
	Epoxy Fracture Surface	0.2523	0.0000	0.0097
	Unbonded Polyimide	0.1759	0.0664	0.0000
	Polyimide Fracture Surface	0.1739	0.0671	0.0000

The fracture surfaces of the ADCB samples for the unfilled and filled bisphenol A, Loctite 3563, and Zymet X6-82-5LV underfills can be seen in Figure 4.1 through Figure 4.4. The cracks direction for all images is from bottom to top.

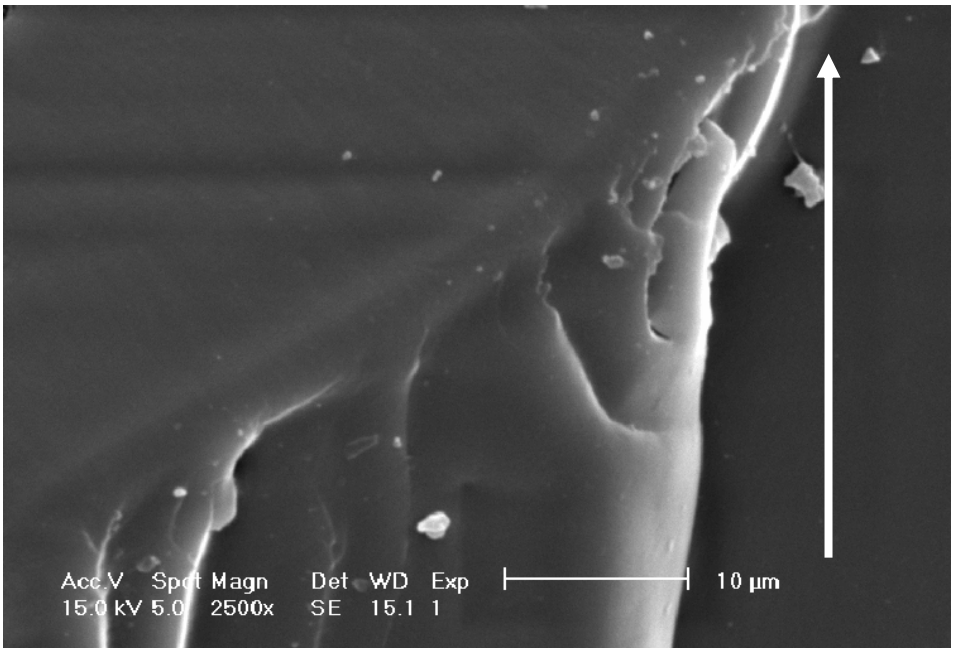

Figure 4.1: Fracture surface of the bisphenol A/T-403 (unfilled)/polyimide ADCB specimen.

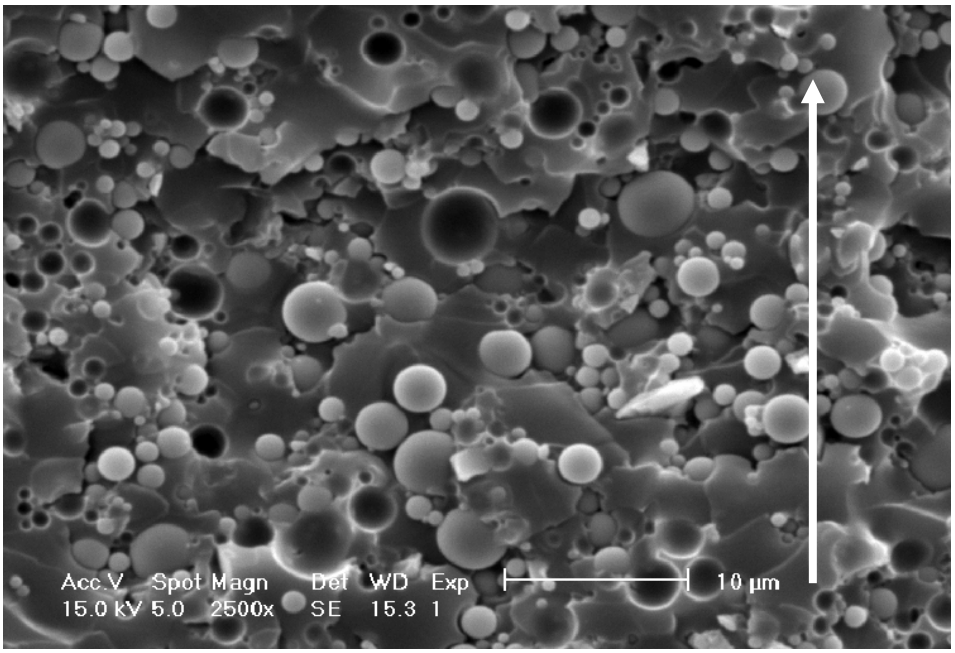

Figure 4.2: Fracture surface of the bisphenol A/T-403 (filled)/polyimide ADCB specimen.

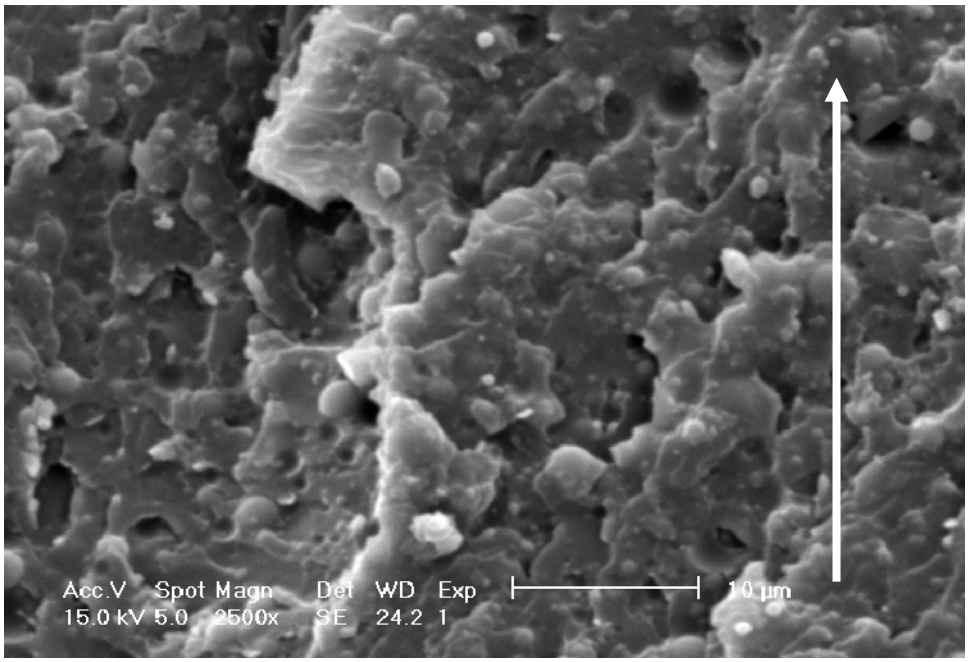

Figure 4.3: Fracture surface of the Loctite 3563/polyimide ADCB specimen.

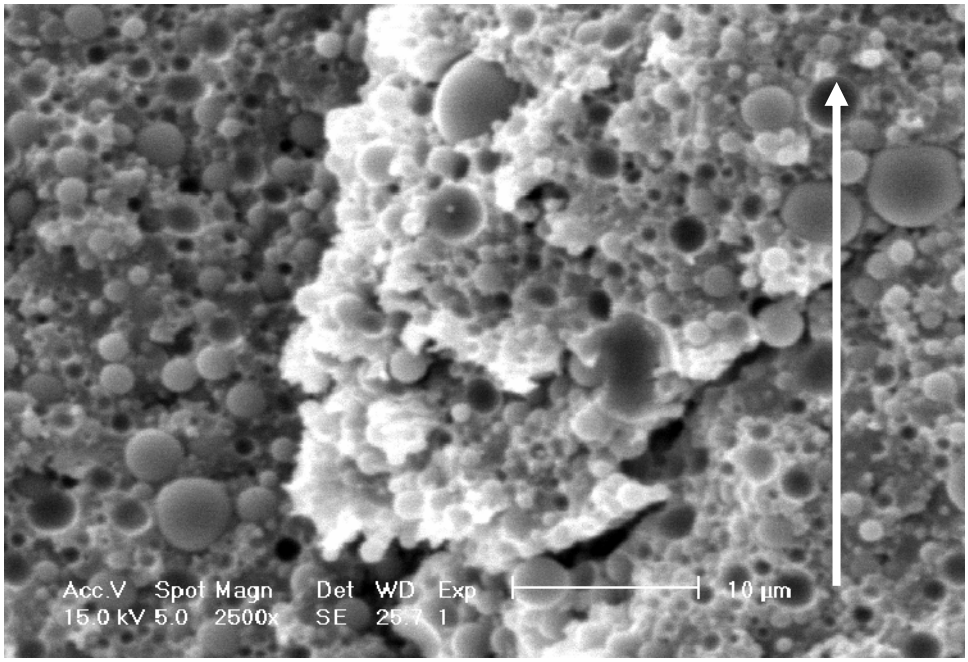

Figure 4.4: Fracture surface of the Zymet X6-82-5LV/polyimide ADCB specimen.

The unfilled bisphenol A material surface contains striations, which is indicative of microcracking. The filled bisphenol A and Zymet material both show weak matrix/particle bonding, while the Loctite material exhibited strong matrix/particle bonding and indications of

the crack pinning. These results confirm that the dissipation mechanisms can enhance the interfacial fracture toughness, provided that the molecular interactions are sufficient for them to operate.

4.2 Stress Singularity Testing

4.2.1 Tensile Butt Joint Testing

Critical stress intensity values were measured for the three model and three commercial underfill systems bonded to both aluminum and the polyimide-coated aluminum surfaces. The results were compared to the ADCB results from Table 4.1 and are presented in Table 4.3. It was assumed for the sake of comparison that all of the material sets used in the testing exhibited the same singularity strength and could be characterized by the same nondimensional calibration factor $A(\alpha,\beta)$. The calibration factor and singularity order used was for a thin epoxy layer bonded to aluminum, with Dundur's parameters of $\alpha = 0.902$ and $\beta = 0.207$ [54]. The underfills tested exhibited the following ranges: $0.750 \leq \alpha \leq 0.936$ and $0.170 \leq \beta \leq 0.215$, corresponding to singularity strengths estimated to range between 0.22 to 0.28 using the results published by Bogy [74].

Table 4.3: Comparison between ADCB and TBJ test results.

Surface	*6061-T6 Aluminum*		*PI-2555 Polyimide*	
Underfill	K_{FEC} *(MPa-mm$^{0.268}$)*	K_{DTC} *(MPa-m$^{0.5}$)*	K_{FEC} *(MPa-mm$^{0.268}$)*	K_{DTC} *(MPa-m$^{0.5}$)*
Bis. A/T-403 (Unfilled)	22.39 ± 1.57	0.94 ± 0.02	20.87 ± 1.26	0.89 ± 0.02
Bis. A/T-403 (Filled)	24.54 ± 1.36	1.46 ± 0.04	22.50 ± 1.28	1.35 ± 0.02
Bis. F/2,4-EMI (Unfilled)	9.44 ± 0.79	0.49 ± 0.03	9.01 ± 0.57	0.42 ± 0.02
Bis. F/2,4-EMI (Filled)	12.03 ± 0.85	0.73 ± 0.03	9.87 ± 0.78	0.61 ± 0.03
Cyclo./Anh. (Unfilled)	10.88 ± 0.51	0.51 ± 0.04	7.33 ± 0.69	0.38 ± 0.02
Cyclo./Anh. (Filled)	6.72 ± 0.77	0.50 ± 0.02	4.81 ± 0.53	0.40 ± 0.05
Dexter FP-4531	10.66 ± 1.01	0.70 ± 0.03	9.44 ± 0.79	0.69 ± 0.04
Loctite 3563	15.86 ± 1.16	1.04 ± 0.02	15.09 ± 0.88	1.01 ± 0.01
Zymet X6-82-5LV	17.71 ± 1.32	1.58 ± 0.05	16.79 ± 1.15	1.50 ± 0.02

The Dundurs' parameters and the corresponding singularity strength can be found in Table 4.4. With the exception of the Dexter and Zymet materials, the assumption of a 0.268 singularity strength seems reasonable for the tested materials. The effect of the lower calculated singularity order for the Dexter and Zymet material are unknown, however due to lack of a calculated calibration factor and for comparison purposes, the same analysis was applied to these as well. The free-edge critical stress intensity factors exhibit a similar ranking to that seen for the ADCB and FC-DT testing. Comparisons of the ADCB and TBJ results can be seen in Figure 4.5.

The critical free-edge stress intensity factors from the TBJ test and the critical strain energy release rates from the ADCB tests correlate well, exhibiting a power trend with a goodness of fit of 0.9564. Converting the energy release rates to crack-tip stress intensity factors using equation (2.11), and comparing the results to the free-edge stress intensity factors, results in a relatively linear trend with a goodness of fit of only 0.6246. Most of the data is linear, however the unfilled bisphenol A and the Zymet material deviate significantly from the curve. Incidentally, the unfilled bisphenol A and the Zymet material exhibit the lowest and highest elastic moduli respectively, and when the strain energy release rates are converted to stress intensity factors, the result is a rearranging of the interfacial fracture toughness rankings.

Table 4.4: Dependence of singularity on Dundurs' parameters [74].

Underfill	ν	α	β	$\alpha(\alpha-2\beta)$	$1-\lambda$
Bis. A/T-403 (Unfilled)	0.350	0.936	0.215	0.473	0.28
Bis. A/T-403 (Filled)	0.345	0.873	0.206	0.404	0.26
Bis. F/2,4-EMI (Unfilled)	0.350	0.923	0.212	0.461	0.28
Bis. F/2,4-EMI (Filled)	0.345	0.869	0.205	0.400	0.26
Cyclo./Anh. (Unfilled)	0.350	0.928	0.213	0.466	0.28
Cyclo./Anh. (Filled)	0.345	0.872	0.205	0.403	0.26
Dexter FP-4531	0.325	0.798	0.207	0.305	0.23
Loctite 3563	0.350	0.864	0.198	0.405	0.26
Zymet X6-82-5LV	0.325	0.754	0.196	0.273	0.22

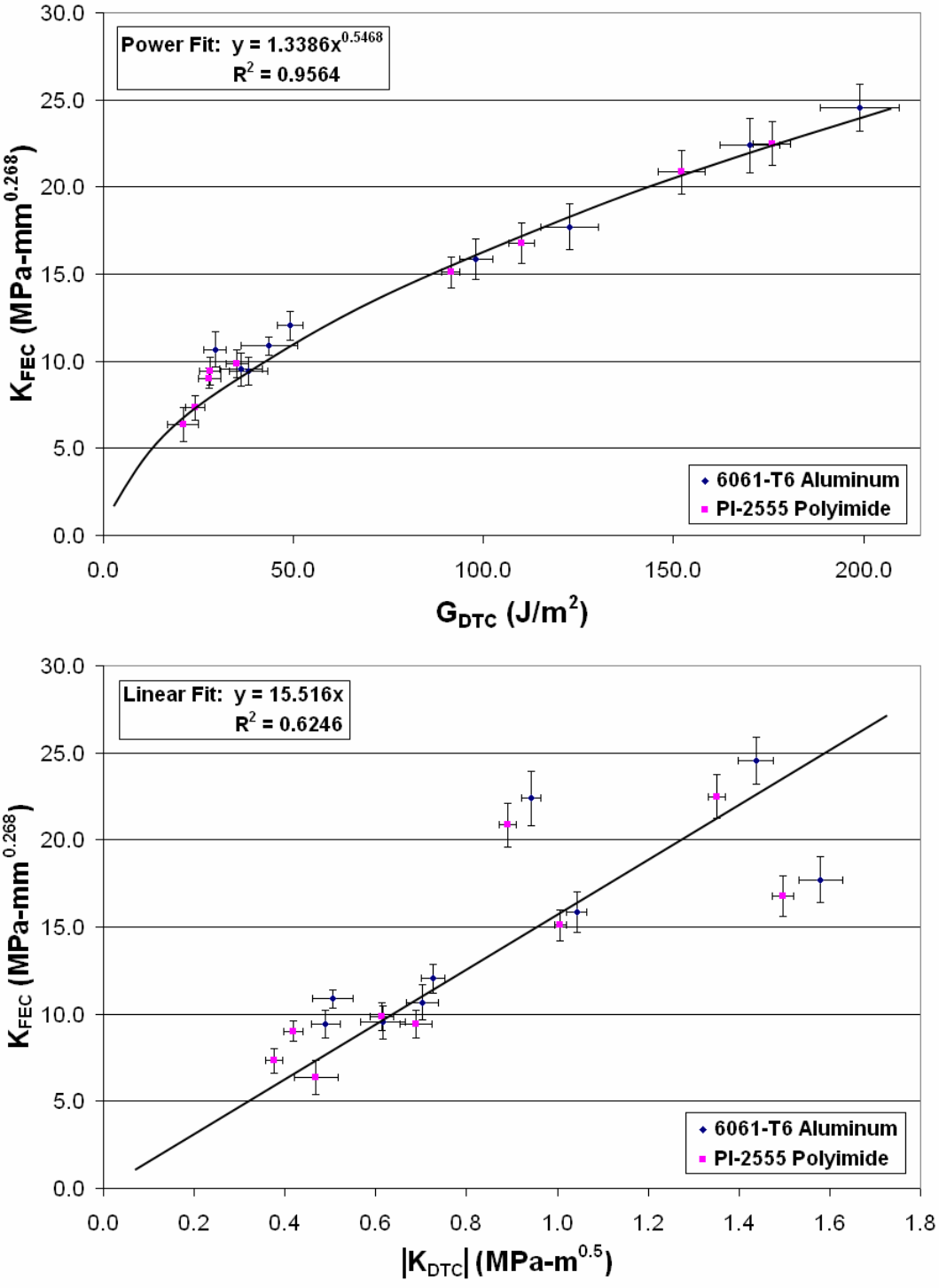

Figure 4.5: Comparison of adhesion results: ADCB and TBJ results correlate well.

The experimental correlation between the ADCB and TBJ results is consistent with other investigations. A relationship between the stress intensity factors for a free-edge and an interfacial crack has been determined both numerically and theoretically by Ioka and Kubo [75]. The study showed that the two approaches should be proportional. This was confirmed earlier by Reedy, who compared an asymptotic small-scale cracking solution to the interface free-edge analysis [61]. It was concluded that the two approaches were equivalent. In fact, the relationship led to the development of an energy release rate relation for a TBJ specimen assuming the presence of inherent interfacial cracks at the free edge. The energy release rate was shown to be dependent on the inherent crack length and the critical free-edge stress intensity factor:

$$G_{DTC} = \frac{\left(1-\beta^2\right)}{E^*} K_{FEC}^2 a^{2\lambda-1} D(\alpha,\beta) \qquad \textbf{(4.1)}$$

where $D(\alpha,\beta)$ is a non-dimensional function involving the Dundurs' elastic mismatch parameters. Although the equation shows the relationship between interfacial failure at a crack and a free-edge, it was emphasized that the inherent flaw and interfacial fracture toughness had limited physical significance for the tensile butt joint, where for a particular calculated free-edge stress intensity factor, any arbitrarily chosen inherent flaw size could be used to generate an energy release rate.

4.2.2 Self-Assembled Monolayer TBJ Testing

As a complement to the underfill/polyimide TBJ testing and to study the effects of molecular interactions on interfacial fracture, TBJ specimens with bisphenol A/T-403 bonded to a controlled organosilane interface were characterized. With the testing performed using the identical organosilane variation as Reedy *et al*. [67], a comparison between the ADCB and TBJ tests could be performed for an additional interface. The results of the testing and the corresponding ADCB results can be seen in Table 4.5.

Table 4.5: Measured interfacial fracture toughness values for varying levels of bromine content.

Percent Bromine	K_{FEC} (MPa-mm$^{0.268}$)	ADCB Testing [67]	
		G_{DTC} (J/m^2)	K_{DTC} (MPa-m$^{0.5}$)
0	2.48 ± 0.31	2.00 ± 0.59	0.11 ± 0.06
10	2.96 ± 0.16	5.90 ± 0.00	0.20 ± 0.00
20	3.90 ± 0.33	4.60 ± 0.00	0.17 ± 0.00
30	5.25 ± 0.32	7.70 ± 1.27	0.23 ± 0.02
40	6.50 ± 0.76	22.55 ± 0.64	0.39 ± 0.01
50	6.96 ± 0.35	18.36 ± 2.84	0.35 ± 0.03
60	8.09 ± 0.60	23.40 ± 2.12	0.39 ± 0.02
70	8.66 ± 0.85	25.65 ± 1.91	0.41 ± 0.02
80	10.17 ± 0.69	35.10 ± 0.42	0.48 ± 0.00
90	11.24 ± 0.56	36.65 ± 5.44	0.49 ± 0.04
100	11.68 ± 0.79	N/A	N/A

The results indicate a very linear relationship between the critical stress intensity factor and the percent bromine (see Figure 4.6), similar to the results seen by Reedy *et al.* for the ADCB testing.

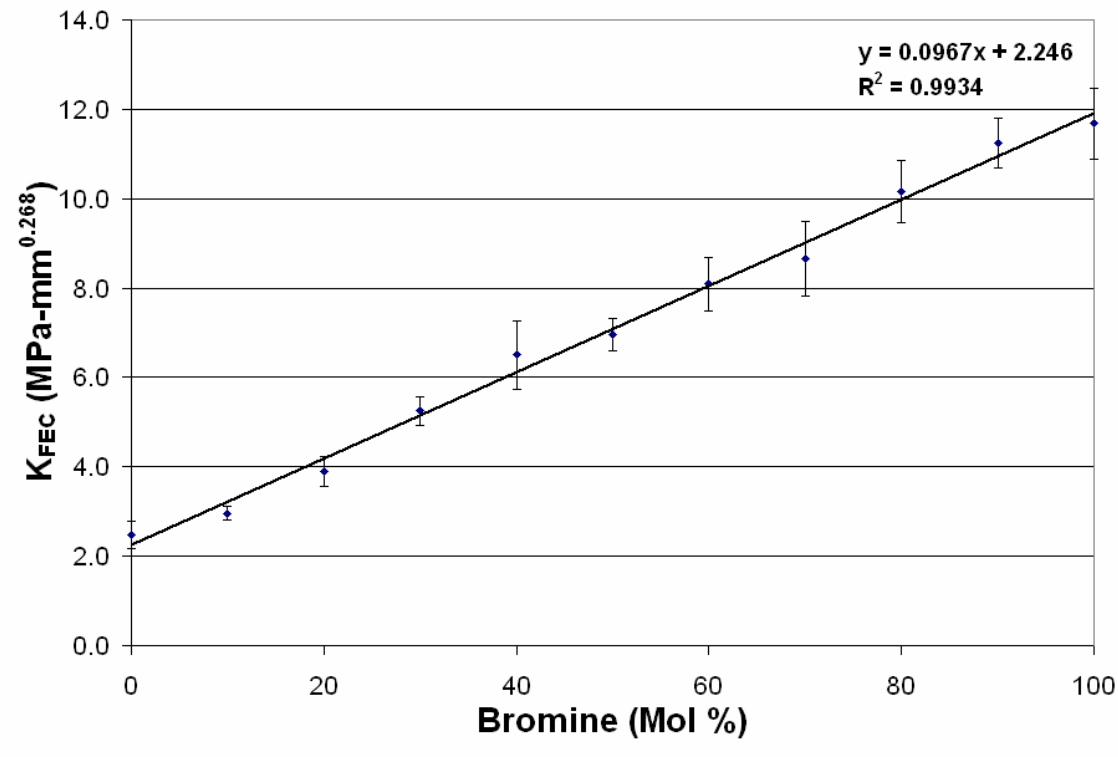

Figure 4.6: Plot of critical free-edge stress intensity factors vs. mole percent bromine in DDTS/BrUTS organosilane.

Accordingly, two important conclusions can be drawn. The first is that the results serve to show that the molecular interactions have a direct relationship with practical adhesion. The second is that the results, compared to the entirety of the TBJ and ADCB data, show a close correlation between the initiation and propagation phenomena. This can be seen more clearly in Figure 4.7, where the SAM results are plotted against the TBJ vs. ADCB underfill data.

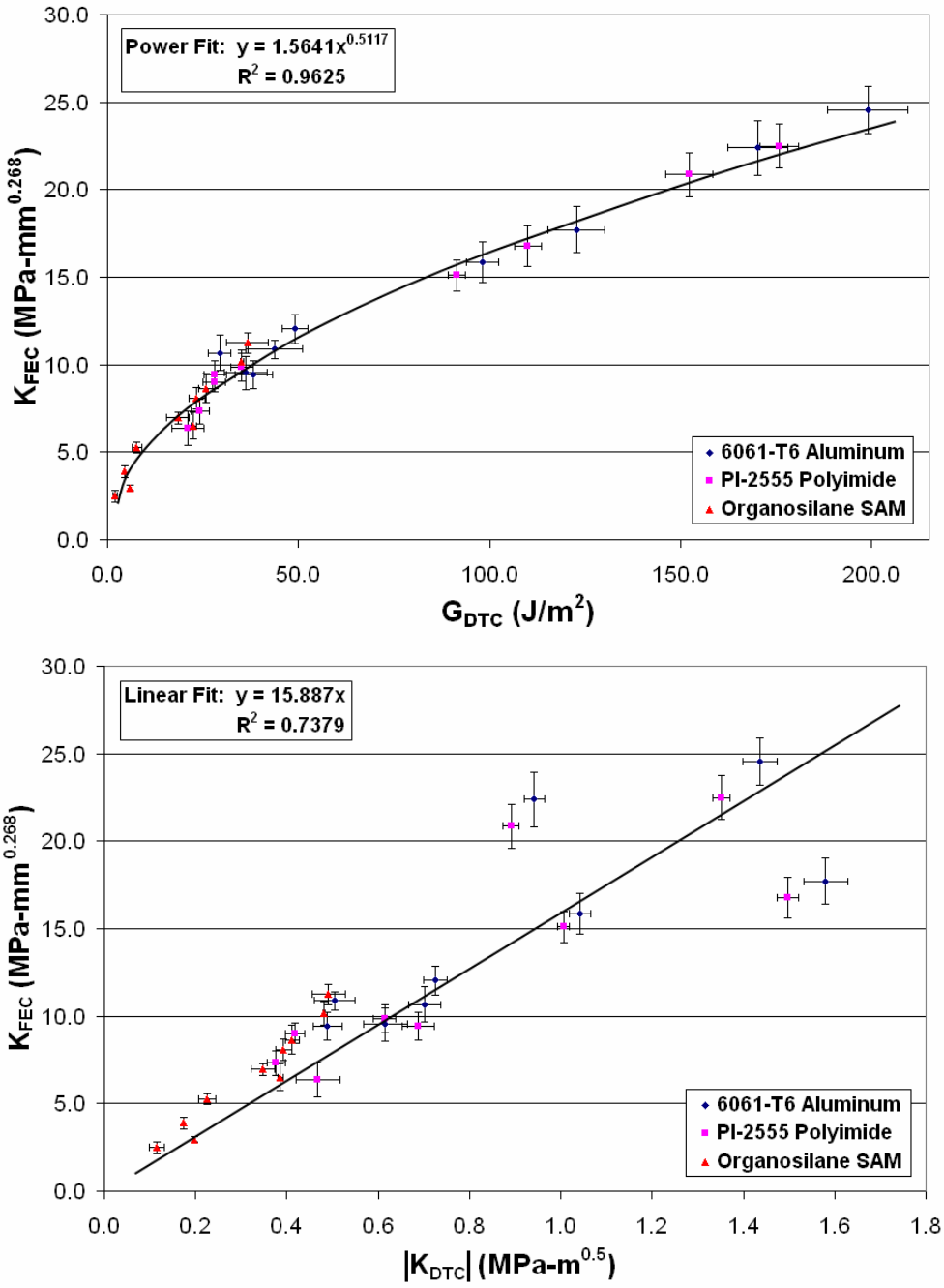

Figure 4.7: Comparison of results from ADCB and TBJ tests, including SAM results.

4.2.3 Verification of TBJ Methodology

Two critical issues needed to be addressed to uphold the validity of the TBJ results: that cracks did not initiate prior to catastrophic failure of the joints (for weaker interfaces) and that significant plastic deformation was not occurring in the vicinity of the free-edge singularity (for

stronger interfaces). Both would invalidate the K_{FEC} criterion. To test that the measured K_{FEC} was in fact an interfacial parameter, the thickness dependence of TBJ samples with both the bisphenol A/T-403 bonded to the 100% DDTS organosilane surface (K_{FEC} = 2.48 MPa-mm$^{0.268}$) and the bisphenol A/T-403 bonded to the aluminum surface (K_{FEC} = 24.54 MPa-mm$^{0.268}$) was examined. Given the criterion, K_{FEC} should not vary with the underfill thickness, and the nominal applied tensile stress to cause joint failure should vary according to the free-edge singularity:

$$K_{FEC} \approx \sigma\, h^{1-\lambda} \;\therefore\; \sigma_{h_1} h_1^{1-\lambda} = \sigma_{h_2} h_2^{1-\lambda} \;\Rightarrow\; \frac{\sigma_{h_1}}{\sigma_{h_2}} = \left(\frac{h_2}{h_1}\right)^{1-\lambda} \quad \textbf{(4.2)}$$

Testing of the TBJ samples was performed for underfill bondlines of 0.25, 0.50, 0.75, and 1.00mm. Failure stresses for the joints were taken as a ratio with the failure stress for the 0.25mm bondline samples, and compared to the expected stress ratios for both the free-edge and a crack tip singularity. Results can be seen in Table 4.6. Examination of the results for both interfaces show that measured stresses match with those expected for a free-edge singularity (Figure 4.8). Subsequent calculation of free-edge stress intensity factors show close correlation with values reported in Table 4.3 and Table 4.5, independent of underfill thickness. The results indicate that the failure of the TBJs is accurately characterized by a stress intensity factor for a free-edge. This predictive capability of the bond thickness effect has also been seen in studies performed by Reedy [62], Akisanya [76], and Qian [77].

Table 4.6: TBJ test verification - comparison with both a free-edge and crack-tip singularity.

Bond Thick. (mm)	*Expected*		*K_{FEC} = 2.48*		*K_{FEC} = 24.54*	
	Crack Singularity	*Edge Singularity*	*Measured Stress Ratio*	*Standard Deviation*	*Measured Stress Ratio*	*Standard Deviation*
0.25	1.00	1.00	1.00	N/A	1.00	N/A
0.50	0.71	0.83	0.84	0.07	0.82	0.08
0.75	0.58	0.75	0.73	0.03	0.76	0.05
1.00	0.51	0.69	0.66	0.06	0.70	0.07

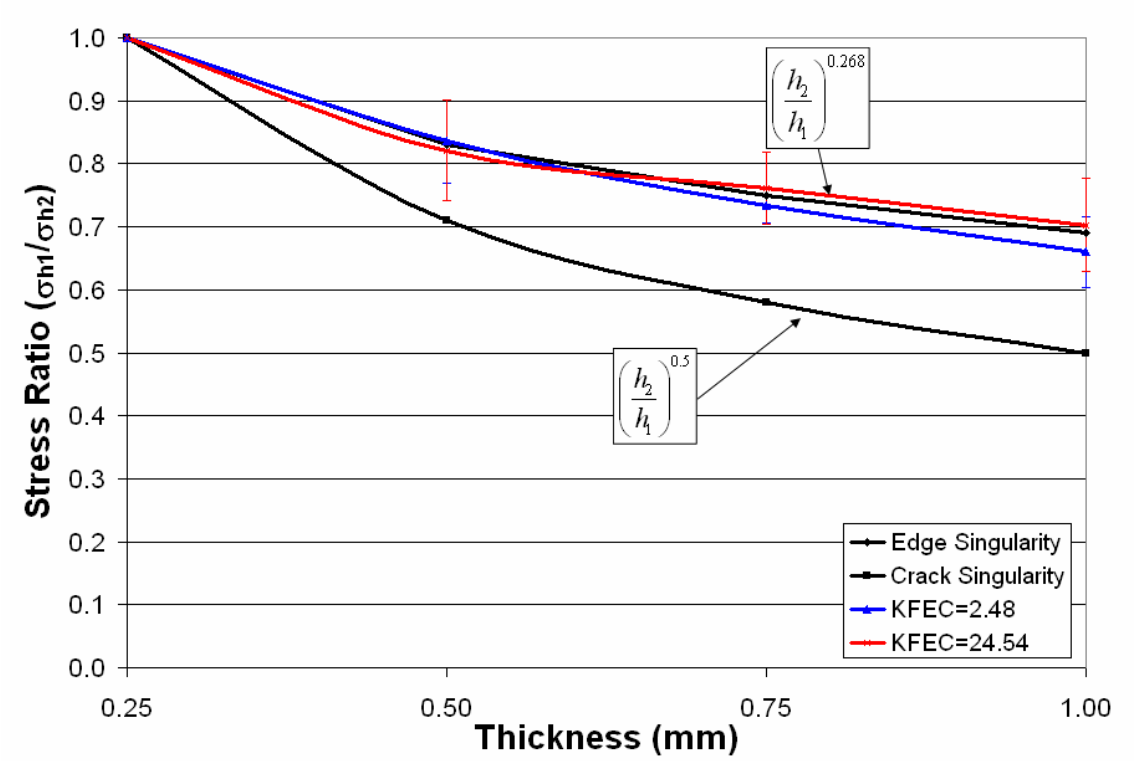

Figure 4.8: Plot of the measured stress ratios compared to the expected values for a free-edge and interfacial crack singularity.

4.2.4 Modified TBJ Testing

The relation between the ADCB and TBJ results show that there is a correlation between interfacial failure for asymptotic geometries associated with different stress singularities. The three commercial underfill systems were tested using modified TBJ geometries to expand on this effect of singularity strength. Joint strengths of samples containing embedded-edge, embedded-corner, and free corner singularities were compared to the strengths measured for the standard free-edge TBJ specimens. The results of the testing can be seen in Table 4.7.

Table 4.7: Joint strengths for the modified TBJ specimen geometries.

Underfill	*Joint Strength (kN)*			
	Embedded Edge	***Free Edge***	***Embedded Corner***	***Free Corner***
Dexter FP-4531	21.37 ± 3.06	19.43 ± 1.63	15.78 ± 2.73	9.43 ± 1.60
Loctite 3563	32.95 ± 2.78	31.07 ± 1.82	27.95 ± 2.87	19.91 ± 2.79
Zymet X6-82-5LV	36.72 ± 2.33	34.55 ± 2.38	28.82 ± 2.01	21.50 ± 3.89

The results show that the ranking of three underfills remains constant for the various geometries, with the Zymet material being the strongest, followed closely by the Loctite underfill, and the Dexter material resulting in the poorest joint strengths. Fracture surfaces indicated that the failures originated at the location of the most severe singularity (see Figure 4.9), with the crack propagating through the fillet for the embedded geometries (see Figure 4.10). The results indicate an increased resistance to initiation by the embedded singularities as compared to their free-surface counterparts, a fact that seems to be more pronounced for the corner singularities over the edge singularities. Additionally, initiation at an edge proves to be more difficult than initiation at a corner. This result seems reasonable, given that the reported singularity strength for a free-corner between a typical epoxy and aluminum is 0.351, significantly higher than the 0.268 for a free-edge [78, 79]. This relation between lower strength and a higher order of singularity has been predicted and shown by several investigators for various applications, including Hattori *et al.* with respect to singularities in plastics encapsulated integrated circuit devices [57], Grenestedt *et al*. on various wedge angles in PVC foam [80], Xu *et al.* on butt vs. convex interfacial joints [81], and Wu on the designing joints to remove stress singularities [82].

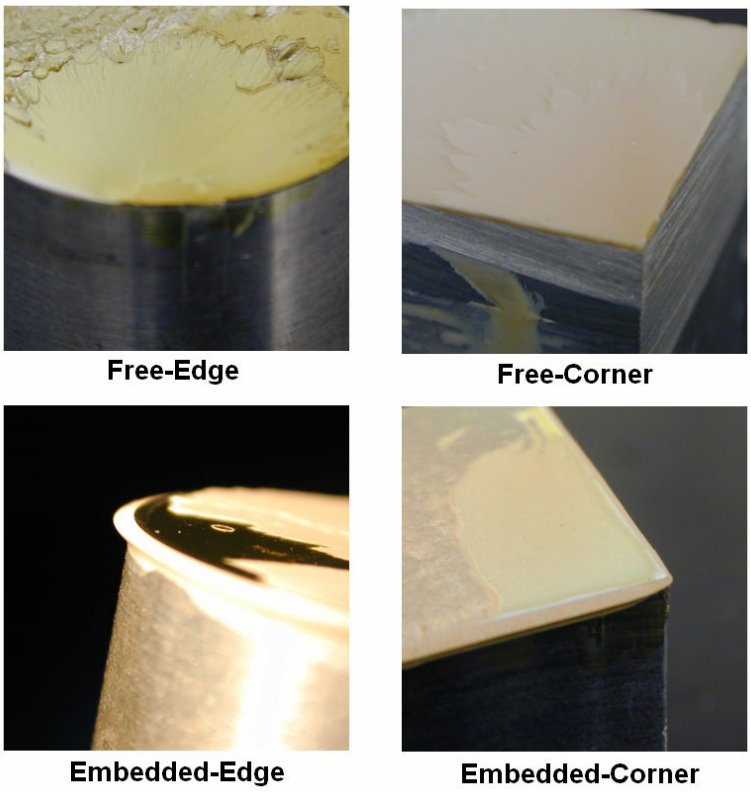

Figure 4.9: Typical initiation sites for the modified TBJ geometries.

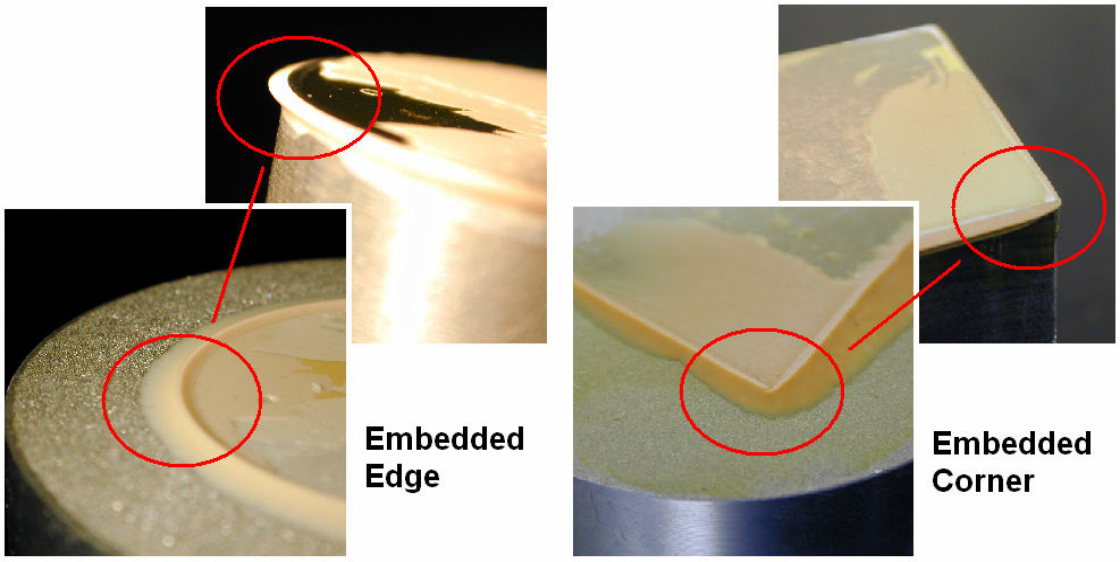

Figure 4.10: Embedded singularity failure locations.

4.3 Fatigue Testing

The results of the monotonic testing of underfill/polyimide interfaces show that practical adhesion can be quantified and understood in terms of both the molecular interactions and the energy dissipation, providing a screening tool for flip-chip underfill selection. However, in reality, underfill materials rarely experience stresses close to that required to cause interfacial failure, and instead are often subjected to repeated loading at these lower levels. The repeated loading can be mechanical in nature, including vibration and shock, as well as induced through thermal excursions. Given the extent of the literature on using monotonic testing to predict flip-chip lifetime, it is extremely important to establish the relationship between sub-critical and critical failure behavior in order to justify their use.

4.3.1 TBJ Fatigue Lifetime Studies

Mechanical fatigue of TBJ samples was performed for the three commercial underfill materials on polyimide. Starting with the monotonic TBJ critical stresses for each of the three materials as a single cycle failure, samples were tested in fatigue at various lower stress levels until catastrophic failure occurred. A plot of the stress levels versus the resulting number of cycles to failure (S-N curves) can be seen in Figure 4.11.

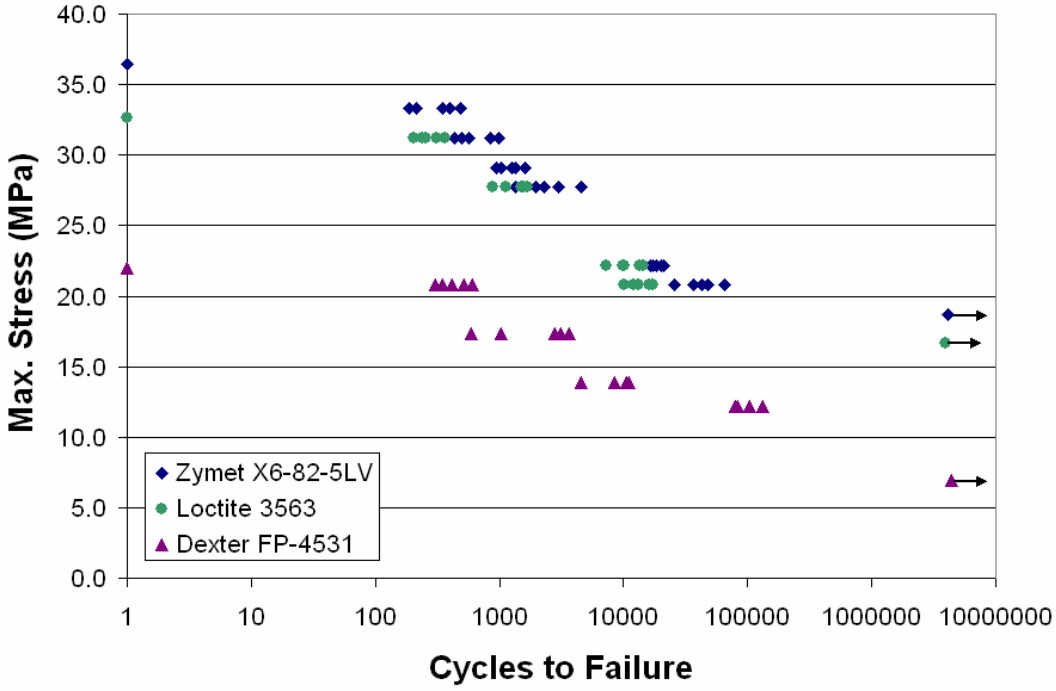

Figure 4.11: Plot of stress versus log of cycles-to-failure data for TBJ specimens (T=25°C, R=0.1).

The S-N curves for the three underfill materials all exhibit a similar sigmoidal shape. Ignoring the monotonic results, a fit of the curves to an equation of the form ($N = kS^{-b}$) shows that the curves have a similar curvature (b), and are mostly distinguishable by a horizontal shift (k). The estimated k and b values can be seen in Table 4.8. Results seem to indicate that the monotonic results provide an accurate indication of the level of expected fatigue behavior.

Table 4.8: Curve fitting parameters for the S-N results.

	k	b
Zymet X6-82-5LV	57.167	0.0947
Loctite 3563	55.098	0.0994
Dexter FP-4531	35.53	0.0957

CHAPTER 5 – CONCLUSIONS

This research was undertaken to improve the understanding of underfill adhesion issues in flip-chip microelectronic assemblies. The pursuit of this goal was divided into two distinct parts: a comparison of the effect of differing geometric discontinuities (which are associated with differing stress singularities) on interfacial fracture and a comparison of the relationship between sub-critical and critical interfacial failure. The first aspect examined the relationship between the interfacial fracture toughness measured for a propagating underfill/passivation disbond and the critical stress intensity factor at a free-edge of the underfill/polyimide interface. A correlation would support the use of fracture mechanics to predict reliability. The second part compared the monotonic adhesion results to the lifetimes of interfaces subjected to cyclic loading. The intention was to provide insight into the utility of using quick single-cycle testing to predict the underfill/polyimide response to being subjected to thermal and mechanical fatigue over a long time frame. Based on these findings, the following conclusions have been drawn.

5.1 Stress Singularities and Practical Adhesion

A comparison between the propagation of disbonds in the asymmetric double cantilever beam testing and the initiation of disbonds in the free-edge tensile butt joint geometry reveled a relationship between the interfacial failure at these two distinct geometric discontinuities (which correspond to different stress singularities). A power trend provided a very good fit to the correlation of the critical energy release rates to the critical stress intensity factors. In addition, the three commercial underfill materials were tested using three modified butt tensile joint geometries containing an embedded edge, a free corner and an embedded corner respectively. The results showed a decrease in joint stress with the increase of singularity severity, with the same underfill interfacial strength ranking for all of the singularities. A key conclusion to be drawn from the results is that failures at a particular interface are related, regardless of the relevant geometric discontinuity. This provides credibility to the continued use of fracture mechanics to provide relative predictions of underfill failure even at small length scales.

5.2 Sub-Critical vs. Critical Initiation

The fatigue results indicate that there is a relationship between critical and sub-critical failure. Comparison of the S-N curves generated for the tensile butt joint samples shows that the lifetime behavior for the three commercial underfills was similar, where the sub-critical failure stress levels of the underfills for a particular lifetime showed a ranking that corroborated with the monotonic tensile butt joint results. The designated threshold stress levels (where all three underfills exhibited at least one million cycles) all fell in the ranking seen for the one-cycle testing.

REFERENCES

1. Soane, D.S. and Z. Martynenko, *Polymers in Microelectronics: Fundamentals and Applications*. Amsterdam: Elsevier Science, 1989.

2. Lau, J.H., *Thermal Stress and Strain in Microelectronics Packaging*. New York: Van Nostrand Reinhold, 1993.

3. Lau, J.H. and Y.-H. Pao, eds. *Solder Joint Reliabilty of BGA, CSP, Flip Chip and Fine Pitch SMT Assemblies*. New York: McGraw-Hill, 1997.

4. Harper, C.A., ed. *Electronic Packaging and Interconnection Handbook*. McGraw-Hill, 2000.

5. Nied, H.F., "Mechanics of Interface Fracture with Applications in Electronic Packaging." *IEEE TDMR*, **3**, 129-143 (2003).

6. Rzepka, S., M.A. Korhonen, E. Meusel, and C.-Y. Li, "The Effect Underfill and Underfill Delamination on the Thermal Stress in Flip-chip Solder Joints." *J. Elect. Pack.*, **120**, 342-367 (1998).

7. Gent, A.N. and J. Shultz, "Effect of Wetting Liquids on the Strength of Adhesion of Viscoelastic Materials." *J. Adhes.*, **3**, 281-294 (1972).

8. Andrews, E.H. and A.J. Kinloch, "Mechanics of Adhesive Failure I." *Proc. Roy. Soc. Lond. A*, **332**, 385-399 (1973).

9. Andrews, E.H. and A.J. Kinloch, "Mechanics of Adhesive Failure II." *Proc. Roy. Soc. Lond. A*, **332**, 401-414 (1973).

10. Maugis, D. and M. Barquins, "Fracture Mechanics and the Adherence of Viscoelastic Bodies." *J. Phys. D: Appl. Phys.*, **11**, 1989-2023 (1978).

11. Cho, K., H.R. Brown, and D.C. Miller, "Effect of a Block Copolymer on the Adhesion Between Incompatible Polymers. I. Symmetric Tests." *J. Poly. Sci. B: Poly. Phys.*, **28**, 1699-1718 (1990).

12. Creton, C., E.J. Kramer, C.-Y. Hui, and H.R. Brown, "Failure Mechanisms of Polymers Interfaces Reinforces with Block Copolymers." *Macromolecules*, **25**, 3075-3088 (1992).

13. Xu, D.-B., C.-Y. Hui, and E.J. Kramer, "Interfacial Fracture and Viscoelastic Deformation in Finite Size Specimens." *J. Appl. Phys.*, **72**, 3305-3316 (1992).

14. Evans, A.G., M. Ruhle, B.J. Dalgleish, and P.G. Charalambides, "The Fracture Energy of Bimaterial Interfaces." *Mater. Sci. Engr.*, **A126**, 53-64 (1990).

15. Komnopad, P. *Fracture Properties of Hybrid Epoxy as Bulk and Adhesive*: 1998.

16. Pearson, R. and P. Komnopad. "Adhesion Studies of Model Epoxy Systems and Commercial Underfill Resins," *Proceedings from the IMAPS International Symposium on Advanced Packaging Materials: Processes, Properties and Interfaces*, 1999.

17. Griffith, A.A., "The Phenomenon of Rupture and Flow in Solids." *Philos. Trans. R. Soc. London*, **A221**, 163-198 (1921).

18. Orowan, E., "Fundamentals of Brittle Behaviour in Metals," in *Fatigue and Fracture of Metals*. Cambridge, MA: MIT Press. p. 139-167, 1950.

19. Irwin, G.R., "Fracture Dynamics," in *Fracturing of Metals*. Cleveland, OH: ASM. p. 147-166, 1949.

20. Irwin, G.R., "Analysis of Stresses and Strains Near the End of a Crack Traversing a Plate." *J. Appl. Mech.*, 361-364 (1957).

21. Sneddon, I.N., "The Distribution of Stress in the Neighborhood of a Crack in an Elastic Solid." *Proc. Roy. Soc. Lond. A*, **187**, 229-260 (1946).

22. Williams, M.L., "On the Stress Distribution at the base of a Stationary Crack." *J. Appl. Mech.*, **24**, 109-114 (1957).

23. Sih, G.S., "Strength of Stress Singularities at Crack Tips for Flexural and Torsional Problems." *J. Appl. Mech.*, **85**, 419-425 (1963).

24. Sih, G.C., P.C. Paris, and G.R. Irwin, "On Cracks in Rectilinearly Anisotropic Bodies." *Int. J. Fract. Mech.*, **1**, 189-203 (1965).

25. Hertzberg, R.W., *Deformation and Fracture Mechanics of Engineering Materials: Fourth Edition*. Fourth ed. New York: John Wiley and Sons, 1996.

26. McClintock, F.A. and G.R. Irwin, "Plasticity Aspects of Fracture Mechanics." *Fracture Toughness Testing and Its Applications, ASTM STP 381*, 84-113 (1965).

27. Rice, J.R., "Elastic Fracture Mechanics Concepts for Interfacial Cracks." *J. Appl. Mech.*, **55**, 98-103 (1988).

28. Hutchinson, J.W. and Z. Suo, "Mixed Mode Cracking in Layered Materials," in *Advances in Applied Mechanics*, J. W. Hutchinson and T. Y. Wu, Editors. New York: Academic Press, Inc. p. 63-191, 1992.

29. Suga, T., E. Elssner, and S. Schmander, "Composite Parameters and Mechanical Compability of Material Joints." *J. Comp. Mat.*, **22**, 917-934 (1988).

30. Dundurs, J., "Edge-Bonded Dissimilar Orthogonal Elastic Wedges Under Normal and Shear Loading." *J. Appl. Mech.*, **36**, 650-652 (1969).

31. Klingbeil, N.W. and J.L. Beuth, "On the Design of Debond-Resistant Bimaterials. Part II: A Comparison of Free-Edge and Interface Crack approaches." *Eng. Fract. Mech.*, **66**, 111-128 (2000).

32. Erdogan, F., "Stress Distribution in Bonded Dissimilar Materials with Cracks." *J. Appl. Mech.*, **32**, 403-410 (1965).

33. Malyshev, B.M. and R.L. Salganik, "The Strength of Adhesive Joints Using the Theory of Fracture." *Int. J. Fract. Mech.*, **5**, 114-128 (1965).

34. England, A.H., "A Crack Between Dissimiliar Media." *J. Appl. Mech.*, **32**, 400-402 (1965).

35. Suo, Z. and J.W. Hutchinson, "Sandwich Test Specimens for Measuring Interface Crack Toughness." *Mater. Sci. Engr.*, **A107**, 135-143 (1989).

36. Suo, Z., G. Bao, and B. Fan, "Singularities, Interfaces and Cracks in Dissimilar Anisotropic Media." *Proc. Roy. Soc. Lond. A*, **427**, 331-358 (1990).

37. Kruzic, J.J., R.A. Marks, M. Yoshiya, A.M. Glaeser, R.M. Cannon, and R.O. Ritchie, "Fracture and Fatigue Behavior at Ambient and Elevated Temperatures of Alumina Bonded with Copper/Niobium/Copper Interlayers." *J. Am. Ceram. Soc.*, **85**, 2531-2541 (2002).

38. Yan, X. and R.K. Agarwal, "Two Test Specimens for Determining the Interfacial Fracture Toughness in Flip-Chip Assemblies." *J. Elect. Pack.*, **120**, 150-155 (1998).

39. Wang, J.S. and Z. Suo, "Experimental Determination of Interfacial Toughness Using Brazil-Nut Sandwich." *Acta Met.*, **38**, 1279-1290 (1990).

40. Liechti, K.M. and Y.S. Chai, "Biaxial Loading Experiments for Determining Interfacial Fracture Toughness." *J. Appl. Mech.*, **58**, 680-687 (1991).

41. Lui, S., Y. Mei, and T.Y. Wu, "Bimaterial Interfacial Crack Growth as a Function of Mode-Mixity." *IEEE Transactions on Components, Packaging and Manufacturing Technology: Part A*, **18**, 618-625 (1995).

42. Charalambides, P.G., J. Lund, A.G. Evans, and R.M. McMeeking, "A Test Specimen for Determining the Fracture Resistance of Bimaterial Interfaces." *J. Appl. Mech.*, **56**, 77-82. (1989).

43. Matthews, F.L. and R.D. Rawlings, *Composite Materials: Engineering and Science*. Cambridge, England: Woodhead Publishing, 1999.

44. Reeder, J.R. and J.R. Crews., "Mixed-Mode Bending Method for Delamination Testing." *AIAA Journal*, **28**, 1270-1276

45. Williams, M.L., "Stress Singularities Resulting from Various Boundary Conditions in Angular Corners of Plates in Extension." *J. Appl. Mech.*, **19**, 526-528 (1952).

46. Bogy, D.B., "Edge-Bonded Dissimilar Orthogonal Elastic Wedges Under Nornal and Shear Loading." *J. Appl. Mech.*, **35**, 460-466 (1968).

47. Gradin, P.A., "A Fracture Criterion for Edge-Bonded Bimaterial Bodies." *J. Comp. Mat.*, **16**, 448-456 (1982).

48. Groth, H.L. and I. Brottare, "Evaluation of Singular Intensity Factors in Elastic-Plastic Materials." *J. Test. Eval.*, **16**, 291-297 (1988).

49. Grenestedt, J.L. and S. Hallstrom, "Crack Initiation from Homogeneous and Bimaterial Corners." *J. Appl. Mech.*, **64**, 811-818 (1997).

50. Rudge, M.R., "Interfacial Stress Singularities in a Bimaterial Wedge." *Int. J. Fract.*, **63**, 21-26 (1993).

51. Zhang, N.S. and P.F. Joseph, "A Nonlinear Finite Element Eigenanalysis of Singular Plane Stress Fields in Bimaterial Wedges Including Complex Eigenvalues." *Int. J. Fract.*, **90**, 175-207 (1998).

52. Reedy, E.D. and T.R. Guess, *Int. J. Fract.*, **98**, L3-L8 (1999).

53. Reedy, E.D. and T.R. Guess, "Butt Joint Strength: Effect of Residual Stress and Stress Relaxation." *J. Adhes. Sci. Tech.*, **10**, 33-45 (1996).

54. Reedy, E.D., "Strength of Butt and Sharp-Cornered Joints," in *Comprehensive Adhesion Science: The Mechanics of Adhesion, Rheology of Adhesives and Strength of Adhesive Bonds*, A. Pocius and D. Dillard, Editors. Amsterdam: Elsevier Science, 2002.

55. Groth, H.L., "Stress Singularities and Fracture at Interface Corners in Bonded Joints." *Int. J. Adhesion Adhesives*, **8**, 107-113 (1988).

56. Hattori, T., S. Sakata, and G. Murakami, "A Stress Singularity Parameter Approach for Evaluating the Interfacial Reliability of Plastic Encapsulated LSI Devices." *J. Elect. Pack.*, **111**, 243-248 (1989).

57. Hattori, T., S. Sakata, and T. Watanabe, "A Stress Singularity Parameter Approach For Evaluating Adhesive and Fretting Strength," in *Advances in Adhesively Bonded Joints*, S. Mall, K. M. Liechti, and J. R. Vinson, Editors. New York: ASME. p. 43-50, 1988.

58. Reedy, E.D., "Intensity of the Stress Singularity at the Interface Corner Between a Bonded Elastic Layer and a Rigid Layer." *Eng. Fract. Mech.*, **36**, 575-583 (1990).

59. Reedy, E.D., "Intensity of the Stress Singularity at the Interface Corner of a Bonded Elastic Layer Subjected to Shear." *Eng. Fract. Mech.*, **38**, 273-281 (1991).

60. Reedy, E.D., "Asymptotic Interface Corner Solutions for Butt Tensile Joints." *Int. J. Solids. Struct.*, **30**, 767-777 (1993).

61. Reedy, E.D., "Connection Between Interface Corner and Interfacial Fracture Analysis of an Adhesively-Bonded Butt Joint." *Int. J. Solids. Struct.*, **37**, 2429-2442 (2000).

62. Reedy, E.D. and T.R. Guess, "Comparison of Butt Tensile Strength Data with Interface Corner Stress Intensity Factor Prediction." *Int. J. Solids. Struct.*, **30**, 2929-2936 (1993).

63. Reedy, E.D. and T.R. Guess, "Butt Joint Tensile Strength: Interface Corner Stress Intensity Factor Prediction." *J. Adhes. Sci. Tech.*, **9**, 237-251 (1995).

64. Reedy, E.D. and T.R. Guess, "Interface Corner Stress States: Plasticity Effects." *Int. J. Fract.*, **81**, 269-282 (1996).

65. Reedy, E.D. and T.R. Guess, "Interface Corner Failure Analysis of Joint Strength: Effect of Adherend Stiffness." *Int. J. Fract.*, **88**, 305-314 (1997).

66. Reedy, E.D. and T.R. Guess, "Additional Interface Corner Toughness Data for an Adhesively-Bonded Butt Joint." *Int. J. Fract.*, **98**, L3-L8 (1999).

67. Reedy, E.D., M.S. Kent, and N.R. Moody. "On the Relationship Between the Molecular Work of Separation and Interfacial Fracture Toughness.," *Proceedings from the 26th Annual Meeting of the Adhesion Society*, 2003.

68. Bao, G., S. Ho, Z. Suo, and B. Fan, *Int. J. of Solids and Struct.*, **29**, 1105-1116 (1992).

69. Dunham, W., "Cardano and the Solution of the Cubic," in *Journey Through Genius: The Great Theorems of Mathematics*. New York: John Wiley and Son. p. 133-154, 1990.

70. Hoontrakul, P., *Understanding the Strength of Epoxy/Polyimide Interfaces*, in *Polymer Science and Engineering*. 2003, Lehigh University: Bethlehem, PA.

71. Carre, A. and J. Schultz, "Polymer-Aluminium Adhesion. I. The Surface Energy of Aluminium in Relation to its Surface Energy." *J. Adhes.*, **15**, 151-162 (1983).

72. Emerson, J.A., R.K. Guinta, G.V. Miller, C.R. Sorenson, and R.A. Pearson. "The Effect of Surface Contamination on Adhesive Forces as Measured by Contact Mechanics," *Proceedings from the Mat. Res. Soc. Symp.*, 2000.

73. Luo, S. and C.P. Wong, "Effect of UV/Ozone Treatment on Surface Tension and Adhesion in Electronic Packaging." *IEEE CPT*, **24**, 43-49 (2001).

74. Bogy, D.B., "On the Problem of Edge-Bonded Elastic Quarter-Planes Loaded at the Boundary." *Int. J. Solids. Struct.*, **6**, 1287-1313 (1970).

75. Ioka, S. and S. Kubo, "Relation Between Stress Intensity Factor of a Small Edge Interface Crack and Intensity of Free-Edge Stress Singularity of Bonded Dissimilar Materials." *Key Engr. Mat.*, **261**, 351-356 (2004).

76. Akisanya, A.R. and C.S. Meng, "Initiation of Fracture at the Interface Corner of Bi-Material Joints." *J. Mech. Phys. Solids*, **51**, 27-46 (2003).

77. Qian, Z. and A.R. Akisanya, "An Experimental Investigation of Failure Initiation in Bonded Joints." *Acta Mat.*, **46**, 4895-48904 (1998).

78. Labossiere, P.E.W. and M.L. Dunn, "Fracture Initiation at Three-Dimensional Bimaterial Interface Corners." *J. Mech. Phys. Solids*, **49**, 609-634 (2001).

79. Koguchi, H., "Stress Singularity Analysis in Three-Dimensional Bonded Structures." *Int. J. Solids. Struct.*, **34**, 461-480 (1997).

80. Grenestedt, J.L., S. Hallstrom, and J. Kuttenkeuler, "On Cracks Emanating From Wedges in Expanded PVC Foam." *Eng. Fract. Mech.*, **54**, 445-456 (1996).

81. Xu, L.R., H. Kuai, and S. Sengupta, "Dissimilar Material Joints with and without Free-Edge Stress Singularities: Part I. A Biologically Inspired Design." *Exper. Mech.*, **44**, 608-615 (2004).

82. Wu, Z., "Design Free of Stress Singularities for Bi-Material Components." *Comp. Struct.*, **65**, 339-345 (2004).

Distribution:

1	MS 0123	D. L. Chavez, LDRD office, 01011
1	MS 0384	R. C. Ratzel, 01500
1	MS 0825	W. L. Hermina, 01510
1	MS 0847	P. J. Wilson, 01520
1	MS 0847	J. M. Redmond, 01524
1	MS 0893	J. Pott, 01523
3	MS 0893	E. D. Reedy, Jr., 01523
1	MS 0893	Day file, 01523
2	MS 0899	Technical Library, 04535
3	MS 1245	J. A. Emerson, 02453
1	MS 9018	Central Technical Files, 08945-1
1	MS 9042	E-P Chen, 08770

3 B. J. McAdams
Zymet, Inc.
7 Great Meadow Lane
East Hanover, NJ 07980

3 R, A. Pearson
Materials Science & Engineering
Whitaker Laboratory
5 East Packer Avenue
Bethlehem, PA 18015-3195